University of Crete
Department of Materials Science and Technology

Master Thesis

Fabrication of metallic photonic structures by two-photon polymerization

Vasilantonakis Nikos

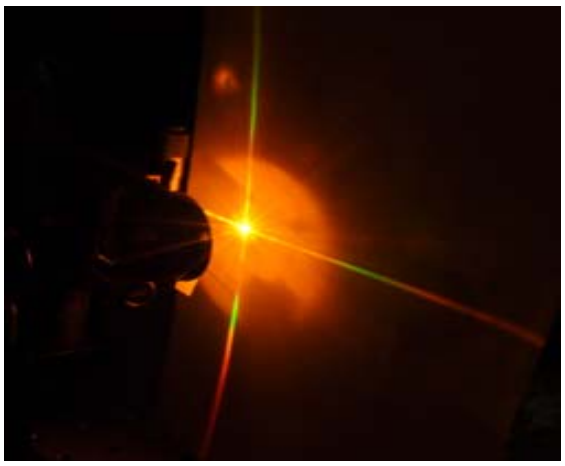

***Advisors*:**
Dr. Maria Kafesaki
Dr. Maria Farsari
Prof. Costas M. Soukoulis

Heraklion, Greece
June 2011

Abstract

During the last few decades there has been an increasing interest for investigation of structures and devices that can control and manipulate light. Such a category of structures are the so-called photonic crystals, i.e. periodic dielectric or metallo-dielectric systems where the diffraction of light can lead to formation of allowed and forbidden spectral regimes for light propagation, known respectively as bands and gaps (or stop-bands).

In this work, we studied the fabrication procedure of a specific category of photonic crystals, named woodpile, using a direct laser writing approach. The main goal was to achieve good quality metallo-dielectric woodpile structures with the smallest possible period (of nm scale). In order to achieve this goal, we fabricated dielectric woodpile structures, (made of a hard polymer that was created in the lab), using a technique called two-photon polymerization (2PP). 2PP is a direct laser writing technique that allows the construction of 3D structures with sub-micron resolution. After fabrication, the dielectric samples were metalized via electroless plating process leading thus to metallic woodpile structures.

Following the aforementioned process we managed to show that our experimental technique is suitable for the fabrication of metallo-dielectric woodpile structures of nanometer scale and quite good structure quality. Specifically, characterizing the morphology of the structures (resolution, average thickness, metal disposition etc.) by varying different fabrication parameters, we showed that resolution below 100 nm can be achieved for 600 nm periodicity structures, and we examined and identified the optimal fabrication conditions as to achieve the highest possible resolution. The electromagnetic characterization of these structures, using transmission measurements, showed the creation of a photonic gap cantered at 450 THz approximately, which was in good agreement with corresponding theoretical results.

Based on metallic woodpile structures like the ones obtained in our work, one can fabricating devices that can reflect light waves over a desired frequency range, allow or forbid light to propagate in certain directions (acting as a waveguide) or confine it in a focal volume (photon localization), which can have huge technological impact.

Table of Contents

Acknowledgements

Foremost, I am grateful to my advisors, Dr. Maria Farsari, Dr. Maria Kafesaki and Prof. Costas Soukoulis for their support and patience throughout the duration of my master research. I would also like to thank George Kenanakis for his help to adapt into the group and his assistance in technical and non-technical matters. My sincere appreciation goes to all the master and PhD students with whom I had the honor to work with. I would especially want to thank Dina Terzaki and Ioanna Sakellari for helping me in my first steps during the metallization and transmission analysis. Without their guidance this work would be impossible.

Chapter 1

Theory of photonic crystals

1.1 History and fundamental properties of photonic crystals

1.1.1 Introduction

Throughout the history of humankind, there have been numerous of breakthroughs that were responsible for the transition of one era to another. These transitions were in close relation with the materials that people used more often in their daily activities. As a consequence, these periods are called Stone Age, Bronze Age, Iron Age, and so forth.

Over the last centuries, there have been enormous improvements towards the electrical properties of the materials. The advances in semiconductor physics, in combination with the description of the electron motion (through the Schrödinger equation), brought the electronic era in our lives. As a result, each device nowadays, needs electricity to function.

However, in the last few decades, a new frontier has emerged. The main purpose in this case is the ability to create structures that can control light. Fabricating devices that can reflect light waves over a desired frequency range, allow light to propagate in certain directions (acting as a waveguide) or confine it in a small volume (photon localization), would definitely have huge technological impacts. Since these materials can manipulate the properties of light, they are called photonic crystals.

1.1.2 Properties of photonic crystals

In this section we are going to introduce the basic properties of the photonic crystals. ***Photonic crystals*** (PhCs) are artificial periodic structures that exhibit spectral gaps in the photonic density of states. The formation of bands (gaps) in PhCs is a result of strong scattering and constructive (destructive) interference of electromagnetic (EM) waves, according to Bragg's diffraction law. The word "crystal" is mainly used because, by definition, a crystal is a periodic arrangement of atoms or molecules. The pattern with which the atoms or molecules are repeated in space is called the ***crystal lattice***.

For example, in the semiconductor a crystal lattice acts as a periodic potential that can prohibit the propagation of certain electron waves. This explains the

formation of ***energy gaps***, meaning that electrons with energies in these gaps can not propagate in specific directions in the crystal. In the case of a strong lattice potential without many defects, the gap can forbid all the propagation directions in a specific frequency range, called thus a ***complete band gap***.

The optical analogue to the previous paragraph is the PhC; here though the atoms or molecules are replaced by macroscopic media with differing dielectric constants (usually two) and the role of the periodic potential is played by a periodic dielectric function. In most cases, PhCs consist of dielectric-dielectric or metallo-dielectric units that repeat in 1, 2 or 3 directions (see Fig. 1). This repetition affects the propagation of EM waves in the same way as the periodic potential in a semiconductor crystal affects the electron motion by defining allowed and forbidden electronic energy bands. However, since now the structure controls the flow of light, we speak about ***photonic band gaps***. Because of the previous definition, PhCs are often called electromagnetic bandgap (EBG) materials or photonic bandgap (PBG) materials. In the special case that a PhC prohibits the EM propagation, over a frequency range, in any direction for both TE and TM polarizations, we say that the crystal has a ***complete or full photonic band gap***.

1.1.3 One-, two-, and three-dimensional photonic crystals

One great advantage of the PhCs is that the periodicity of the crystal can easily change, conversely to the semiconductors in which periodicity is fixed for a given system. Changing the periodicity and the size of elementary PhC building blocks (unit cells) one can change the frequency of operation, obtaining band gaps in the frequency regime of MHz (for cm unit cell size PhCs) to THz (for nm-scale PhCs). One has to note that moving to higher frequencies the periodicity of the crystal has to decrease significantly (more info about this topic in Section 1.1.5). Additionally, as we can see in Fig. 1, the theoretical analysis and, especially, the experimental fabrication techniques of PhCs become more and more frustrating as we move from 1 dimension to 3 dimensions.

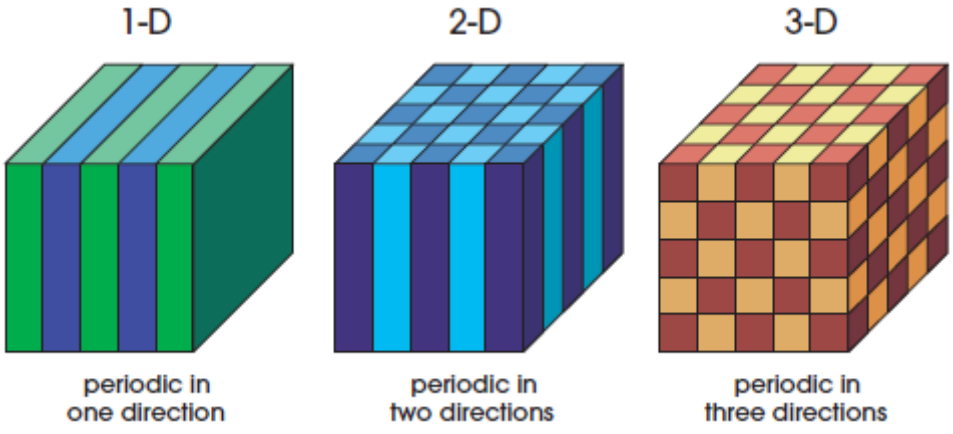

Figure 1: Typical sketches of 1D, 2D and 3D photonic crystals. Different colours correspond to materials with different dielectric constants. Image was adopted from [PC1].

A widely known 1D PhC that is used in many optical devices is the quarter-wave stack reflector (a basic building block of optical thin-film products), that consists of alternating layers of two or more dielectric materials (like the left image of Fig. 1). A beam of a proper wavelength that is incident on such a layered material is completely reflected. The physical explanation of this phenomenon comes from the periodicity of the layers. Each light wave is partially reflected at each layer interface, and since the structure is periodic, the multiple reflections of the incident wave interfere destructively along propagation direction and eliminating the propagating wave; thus we have total reflection. Some other devices that are based on PhCs are the Fabry-Perot filter and the distributed feedback lasers.

A very promising kind of 2D PhC is the photonic-crystal fiber (PCF). PCF is a new class of optical fiber where the waveguiding is based on the properties of photonic crystals. Because of its ability to confine light in hollow cores or with confinement characteristics not possible in conventional optical fibers, PCF is now finding applications in fiber-optics communications, fiber lasers, nonlinear devices, high-power transmission, and highly sensitive gas sensors.

Finally, the most advantageous and, simultaneously, most challenging in fabrication case is that of 3D PhCs. At this point it is good to move a little back in time and mention the first attempts of 3D PhC fabrication. In the end of 1990, a theoretical publication by Ho, Chan, and Soukoulis [1] showed the existence of full PBG in a periodic dielectric structure. The proposed structure had a periodic arrangement of dielectric spheres in a diamond lattice form. However, the fabrication of diamond-like structures is very difficult, especially in the micrometer length scale and below. At the same time, Yablonovitch [2] devised a structure (the well-known Yablonovite structure) that was not diamond-like, but had the same symmetry of a diamond lattice. This was achieved by drilling cylindrical holes through a dielectric block. This structure was the first in history fabricated that depicted complete PBG, in agreement with the theoretical predictions [3]. After this successful attempt, lots of efforts were made in the construction of different unit cells (like spheres in a diamond lattice or inverse colloidal-crystal spheres). However, the most successful synergy between theory and experiment is encountered in so-called woodpile structure, in which this thesis is relying on (read Section 1.1.5 for more information).

In general, the fabrication of PhCs can be either easy or extremely difficult, depending upon the level of dimensionality (the more dimensions the harder the construction) and the desired frequency of the band gap (smaller periodicity means harder fabrication). Additionally, as we shall see in Section 1.1.4, the periodicity of each structure must be on the same order with the wavelength of operation, which simply means that, until to date, the most hard and challenging fabrication task is the fabrication of 3D PhCs in the near-IR and optical regime.

1.1.4 Negative refraction in photonic crystals and metamaterials

This section analyzes a fundamental property of some PhCs, which is the refraction of an incident wave in negative angles (negative refraction). Such PhCs are called ***photonic metamaterials***. By the term ***metamaterials*** (MMs) we characterize artificial systems exhibiting, as a result of their structure, unique properties that are absent in each one of their constituents and in many cases absent in natural materials. The

world metamaterial comes from the Greek word “meta”, which means beyond. Thus, metamaterials donate structures that are beyond the conventional materials.

The term “beyond the conventional materials” usually means that the electrical permittivity and the magnetic permeability of those structures present values that can not be found in nature. Transparent materials (i.e. dielectrics) of the most usual types present positive values for the electrical permittivity $\varepsilon(\omega)$ and for the magnetic permeability $\mu(\omega)$. On the contrary, certain metals and semiconductors, although they have positive magnetic permeability, exhibit negative electric permittivity at specific frequency ranges. On the other hand some antiferromagnetic systems may exhibit negative $\mu(\omega)$ for a limited frequency range, lower than the frequency range of negative $\varepsilon(\omega)$ in metals or semiconductors. These materials are also at the same time very anisotropic. When both $\varepsilon(\omega)$, $\mu(\omega)$ of a given material are positive then the refractive index ($n^2(\omega) = \varepsilon(\omega)\,\mu(\omega)$) is positive too, and the EM wave propagates in the medium with a velocity $c/n(\omega)$. When one of them in negative, the refractive index is imaginary and the EM wave can not propagate in such materials.

Until 1968, no scientist had researched the case where both $\varepsilon(\omega)$ and $\mu(\omega)$ were simultaneously negative, since no material had these properties. Veselago [4] was the first person who, theoretically, studied such materials and predicted many unique and unusual properties in those hypothetical media with negative index being among these properties. In 2000, more than 3 decades later, Smith and his co-workers [5, 6] presented experimental results of structures with both negative $\varepsilon(\omega)$ and $\mu(\omega)$, following theoretical predictions by Pendry [7]. This success has resulted in a breakthrough in the development of metamaterials (MMs). Furthermore, a different approach for achieving negative refractive index, using PhCs, has been proposed [8-13], meaning that these two categories of materials are closely related each other.

At this point, it is reasonable to ask what is the difference between negative index PhCs and MMs, since both of them can show the same effects. In PhCs propagation is governed mainly by diffraction and the operation frequency regime occurs when the wavelength inside the material is comparable to the period (for more information read Ch. 16 of [PC2]). Conversely, the unit cells of MMs are much smaller than the wavelength of operation, making these structures acting as homogeneous media for the waves propagating into them [14]. The reason why both negative index PhCs and MMs are fabricated has to do with the fact that each one has its own advantages and drawbacks. For example, MMs could be used for the miniaturization of devices, since their unit cells are very small, while PhCs, in principle, have smaller absorption losses especially at high frequencies.

The main properties that making negative index PhCs and MMs unique are, briefly, discussed below. a) The Doppler shift is reversed; this means that when a source is moving away from a detector blue shift is observed and vice versa. b) Opposite Cherenkov radiation; in a negative index material the energy flow will be in the direction $-\mathbf{k}$ ($\mathbf{k}$ = wavevector). c) Creation of perfect lenses; Pendry [7] suggested that negative index materials can act as perfect lenses reproducing images of an object with unlimited details, overcoming the diffraction limit. d) The phase velocity is opposite to the group velocity; an immediate physical consequence of this is that the refraction of EM waves at the plane interface of a regular right-handed material (RHM) and a MM would be “negative” (i.e. the refracted wave will be refracted at negative angles). All these properties are thoroughly discussed in many books ([PC2]-[PC4]). Negative index MMs are often called left-handed materials (LHMs), backward mediums or double negative media.

1.1.5 Characteristics of woodpile structures

This work is dedicated to the construction of 3D metallic PhCs. Among 3D lattice structures, the woodpile lattice is one of the most popular because it is simpler than the other possible 3D geometries [15-19]. It was first designed by the Iowa State University (ISU) group [16] and fabricated [20] by stacking alumina cylinders; it showed a complete 3D bandgap at 12 to 14 GHz (microwave region).

Woodpile structures have fcc [PC5] symmetry. The woodpile characteristics, along with the first Brillouin zone for the fcc lattice, are shown in Fig. 2 [21]. The structure consists of layers of one dimensional rods with a stacking sequence that repeats itself every four layers. The unit cell (u.c.) height is c, the rod's width w, and the distance between two adjacent rods (i.e. the periodicity) is d (from center-to-center). Each layer is rotated by 90º compared to its neighboring layers. Between every second layer, the rods are shifted by d/2 (see Fig 2). For the special case of c/d $=\sqrt{2}$, the lattice can be derived from a face-center-cubic (fcc) unit cell with the basis of two rods [22]. Fig. 2(b) demonstrates unit cell of the reciprocal lattice in the fcc case. The colored line depicts the high symmetry points of k-space.

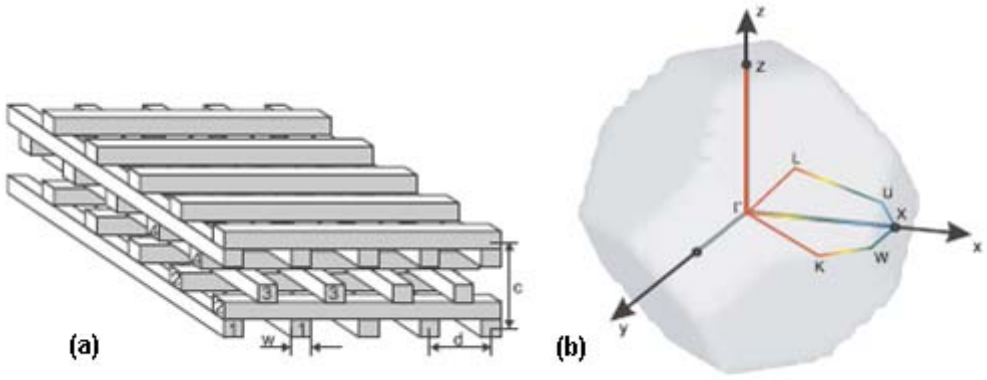

Figure 2: (a): Woodpile structure containing four layers of rods. The symbols w, d and c are for the width of rods, the distance between two adjacent rods and the height of a unit cell respectively. (b): The first Brillouin zone of the fcc woodpile structure. The colored line depicts the high symmetry points of k-space.

1.1.6 Potential applications of PhCs

Up to now, we have seen that 2D PhCs have several potential applications in microfabricated optical fibers [23-25], beam splitters and switches [26,27], microwave planar antennas [28], photonic integrated circuits [29] and so on. However, all the aforementioned applications are mainly function in microwave frequencies or below. One of the most challenging task is to miniaturize PhCs as to operate in the telecommunication regime, and use them in the construction of fully ***photonic integrated circuits*** (PICs). To achieve this goal, 3D PhCs must be fabricated with resonances around 200THz ($\lambda \approx$ 1.5 μm) or higher. If that happens, electronic integrated circuits (EICs), also known as microchips could be replaced by PICs and a

new evolution of communication devices will emerge which will be much faster than the current devices that are on EICs.

One fundamental application of the PICs would be in the creation of **optical computers** (also called photonic computers). An optical computer is a device that uses photons of visible light beams, rather than electrons in an electric current, to perform digital computations. An electric current creates heat in computer systems. As the processing speed requirement increases, so does the amount of electricity required. The resulting heat is extremely damaging to the hardware and is the most critical factor for the decrease of computers' lifetime. Photons, however, create substantially less heat than electrons, on a given size scale. Thus, the development of more powerful processing systems becomes possible. By applying some of the advantages of visible and/or IR networks at the device and component scale, a computer might someday be developed that can perform operations significantly faster than a conventional electronic computer.

Another important application would be the usage of PhCs in order to enhance the emission rate of light sources. In general, spontaneous emission can be controlled by the geometry of the medium surrounding the fluorescent species. There have been many experimental efforts studying the spontaneous emission of emitters that are embedded in PhCs [30-33]. Additionally, it has been shown theoretically [34] that having a dipole emitter inside and even in the near field above the structures a 2D PhC membrane one can increase the spontaneous emission rate by more than ten times compared to vacuum rate, and also can modify the directionality of the emission for a given frequency. Thus, PhCs can achieve many of the long-standing goals of photonic bandgap materials and also shield the source from unwanted interactions.

1.2 Electromagnetism in mixed dielectric-metallic media

In this part, we are going to discuss the basic relations for the electric and magnetic field in the woodpile crystal. As we have seen in section 1.1.5, a woodpile consists of two media, the air (≈vacuum) and the material of the structure, which in our case is silver. Silver metal is particularly appealing because it has high electrical conductivity and shows unique physical properties in the nanometer regime [35, 36]. Our strategy is to find first the wave equation for the EM fields in an arbitrary isotropic homogeneous material. Starting from the four macroscopic Maxwell's equations, in SI units, we have:

$$\begin{aligned} &\nabla\cdot\mathbf{B} = 0 \quad \text{(a)} \quad \nabla\times\mathbf{E} + \frac{\partial\mathbf{B}}{\partial t} = 0 \quad \text{(b)} \\ &\nabla\cdot\mathbf{D} = \rho_{ext} \quad \text{(c)} \quad \nabla\times\mathbf{H} - \frac{\partial\mathbf{D}}{\partial t} = \mathbf{J}_{ext} \quad \text{(d)} \end{aligned} \tag{1}$$

where **E** and **H** are the macroscopic electric and magnetic fields, **D** and **B** are the displacement and magnetic induction fields, and ρ_{ext} and $\mathbf{J}_{ext}$ are the external charge density and current density, respectively, which in our case are zero.

In order to solve the above equations we need to employ appropriate relationships between **E – D** and **H – B**. In general, **D** and **H** are given from the following expressions:

$$\mathbf{D} = \varepsilon_0 \mathbf{E} + \mathbf{P} \tag{2}$$

$$\mathbf{H} = \frac{1}{\mu_0}\mathbf{B} - \mathbf{M} \tag{3}$$

where $\varepsilon_0 \approx 8.854 \times 10^{-12}$ Farad/m is the vacuum permittivity and $\mu_0 = 4\pi \times 10^{-7}$ Henry/m is the vacuum permeability. The **P** and **M** symbols are the polarization and the magnetization fields which are defined in terms of microscopic total charges and currents respectively. At this point three approximations must be made. We assume the material is isotropic, homogeneous and linear so that the **P** is proportional to **E** and **M** is proportional to **H**. Taking this into consideration, one can re-write (2) and (3) according to the following equations:

$$\mathbf{D} = \varepsilon \mathbf{E} \tag{4}$$

$$\mathbf{H} = \frac{1}{\mu}\mathbf{B} \tag{5}$$

where ε, μ are called the electrical permittivity and magnetic permeability, respectively, of a material. For vacuum **P**=0 and $\varepsilon = \varepsilon_0$. For an arbitrary isotropic material the permittivity can be written as $\varepsilon = \varepsilon_0 \varepsilon_r$, where ε_r is a scalar function called the ***relative permittivity***. Likewise, the permeability can also be expressed as $\mu = \mu_0 \mu_r$, where μ_r is called the ***relative permeability***. Depending on the problem both ε_r and μ_r could be constants, functions of space and/or frequency or even tensors. Using equations (4) - (5) the macroscopic Maxwell's equations take the form:

$$\begin{aligned} &\nabla\cdot(\mu\mathbf{H}) = 0 \quad (a) \quad \nabla\times\mathbf{E} + \mu\frac{\partial \mathbf{H}}{\partial t} = 0 \quad (b) \\ &\nabla\cdot(\varepsilon\mathbf{E}) = 0 \quad (c) \quad \nabla\times\mathbf{H} - \varepsilon\frac{\partial \mathbf{E}}{\partial t} = 0 \quad (d) \end{aligned} \tag{6}$$

To continue further, better examination of ε and μ is required. In this work, the material where we consider propagation is silver. Silver is a non-magnetic metal; this means that the relative permeability should be very close to unit ($\mu_r = 1$). In this case the permeability is constant and equal to μ_0. However, this is not correct for the permittivity. In general, the relative permittivity is a function of both space and frequency ($\varepsilon_r = \varepsilon_r(\mathbf{r},\omega)$). In the previous paragraphs, we have made the assumptions that silver is homogeneous (of course in reality there are always some defects on the structures so this case is only an approximation). In this occasion only, ε is

independent of the position **r** ($\varepsilon_r(\mathbf{r},\omega) = \varepsilon_r(\omega)$). For metals, the dielectric function can be approximated by the Drude model:

$$\varepsilon_r(\omega) = 1 - \frac{\omega_p^2}{\omega^2 + i\omega\gamma} = 1 + \frac{i\sigma}{\omega\varepsilon_0} \tag{7}$$

where ω_p, $\gamma = 1/\tau$ and σ are the plasma frequency (the resonance frequency), the collision frequency (τ is the mean free time between electronic collisions) and the conductivity of metal respectively. The Drude model of electrical conduction was proposed in 1900 by Paul Drude to explain the transport properties of electrons in materials with high conductivity, such as metals. The model, which is an application of kinetic theory, assumes that the microscopic behaviour of electrons in a solid may be treated classically. In this state, electrons bounce off heavier relative immobile positive ions (more information in [PC6]). The plasma frequency and the collision frequency for silver are $\omega_p \approx 1.37 \times 10^{16}\ s^{-1}$ and $\gamma = 8.5 \times 10^{13}\ s^{-1}$ [37].

Finally, we should examine the electromagnetic fields and simplify them. In general, **E** and **H** are complicated functions of time and space. However, because the Maxwell equations are linear, time will be independent of space, thus one can write the fields into a set of harmonic modes (so that the fields vary sinusoidally in time). A very common mathematical trick is to write the EM fields as a complex exponential function of time and remembering to take the real part in order to obtain the physical fields (using the Euler formula, $e^{i\theta} = \cos(\theta) + i\sin(\theta)$). The reason is that an exponential function is invariant under derivative transformations and this is very convenient during the calculations. Thus the EM fields can be written:

$$\begin{aligned} \mathbf{H}(\mathbf{r},t) &= \mathbf{H}(\mathbf{r})\exp[-i\omega t] \\ \mathbf{E}(\mathbf{r},t) &= \mathbf{E}(\mathbf{r})\exp[-i\omega t] \end{aligned} \tag{8}$$

Considering all the above, we can modify (6) and derive the final Maxwell equations for a metallic media:

$$\begin{aligned} &\nabla\cdot\mathbf{H}(\mathbf{r}) = 0 \quad (a) \qquad \nabla\times\mathbf{E}(\mathbf{r}) - i\omega\mu_0\mathbf{H}(\mathbf{r}) = 0 \quad (b) \\ &\nabla\cdot(\varepsilon\mathbf{E}(\mathbf{r})) = 0 \quad (c) \qquad \nabla\times\mathbf{H}(\mathbf{r}) + (i\omega\varepsilon_0\varepsilon_r(\omega))\mathbf{E}(\mathbf{r}) = 0 \quad (d) \end{aligned} \tag{9}$$

From the above relations, (9b) and (9d) are functions of both the electric and the magnetic waves. Since $\varepsilon_r(\omega)$ is invariant in space, we can decouple them by taking the curl of (9b) and use (9d) to eliminate **H**(**r**). This will lead us to an equation for the electric field only. Following the opposite direction (taking the curl of (9d) and use the result of (9b) to eliminate **E**(**r**)), we can derive an equation of the magnetic field as an unknown. The results are two independent equations:

$$\nabla\times\nabla\times\mathbf{E}(\mathbf{r}) = (\frac{\omega^2\varepsilon_r(\omega)}{c^2})\mathbf{E}(\mathbf{r}) \tag{10}$$

$$\nabla\times\nabla\times\mathbf{B}(\mathbf{r}) = (\frac{\omega^2\varepsilon_r(\omega)}{c^2})\mathbf{B}(\mathbf{r}) \tag{11}$$

These are the ***wave equations*** in a homogeneous and isotropic metallic material. Although the formulas seem to be complicated, the content of them is very simple: By performing a series of operations on **E**(**r**) or **H**(**r**), the result should be a constant times the original function, in order to be an allowable EM wave. This consequence, explains the harmonic properties of waves. In mathematical physics, the above relations are eigenvalue problems. The simplest solution of this type of problem is plane waves of the form

$$\begin{aligned}\mathbf{E}(\mathbf{r},t) &= \mathbf{E}_0\exp[i(\mathbf{k}\cdot\mathbf{r} - \omega t)]\\ \mathbf{B}(\mathbf{r},t) &= \mathbf{B}_0\exp[i(\mathbf{k}\cdot\mathbf{r} - \omega t)]\end{aligned} \tag{12}$$

where $k = \omega\,\varepsilon_r^{1/2}(\omega)/c$ while $\mathbf{E}_0$ and $\mathbf{B}_0$ are the amplitudes of the electric and the magnetic fields, respectively. It is also worth mentioning that the same solution is valid in the case of a dielectric material (a polymer for example), with one basic difference: The wavevector in an insulator is mainly real, contrary to the metallic material where **k** has a significant imaginary part due to the conductivity that it has (see Eq. (7)). In the case of vacuum, the conductivity tends to zero while the relative permittivity is unit. Replacing $\varepsilon_r(\omega) = 1$ in equations (10) and (11) one can find the wave equations in space ([PC1]).

Now, in order to solve the problem in a mixed dielectric-metallic media we have to use the relations (9) taking into account that the permittivity now is a function of space too. Thus the differential operations will not act only on the fields but also on the permittivity too. This makes analytical solutions rare and generally confined to very simple systems. Thus, computer methods are often used which solve these problems numerically.

Despite the fact that there are lots of different numerical methods, the most widely used are the plane-wave (PW) method, the transfer matrix method (TMM) and the finite-difference time-domain (FDTD) method. All of them can be applied to both PhCs and MMs but each one has its own advantages and disadvantages.

The PW method is basically used to calculate the dispersion relation in infinite periodic systems [38]. It is the fastest and easiest to apply, and the main benefit is the ability to plot the entire frequency spectrum for a given wavevector. Its main disadvantages are the inability to be used it in finite systems, in systems where ε is frequency dependent (dispersive materials), as well as in systems with defects.

Contrary to the PW method, TMM is able to calculate the band structure as **k** varies for a fixed frequency. Furthermore, it is accurate even for dispersive materials with arbitrary shapes and properties, such as lossy metallic structures. TMM however, is less easy to apply than the PW and it also requires the discretization of the unit cell which brings some numerical artifacts and constrains. This method was first proposed by Pendry and MacKinnon [39] in 1992.

Finally, the FDTD method can also be used to visualize the band structure and the scattering properties of PhCs and MMs. The most significant difference here is that, while TMM is employed for steady-state solutions, FDTD method is used for time-dependent solutions. Thus, it can give the transmission properties over a wide frequency range in a single calculation. Additionally, it can plot the time-domain pictures of the fields and the currents over the entire computational domain. FDTD is a very fundamental tool for the study of transmission through finite slabs, the investigation of systems with dielectric or metallic components [40-44], and in materials with nonlinear dielectric properties [45-47]. As for the drawbacks, there are about the same with the TMM, since they mainly have to do with the discretization of the unit cell and the correct time step in the case of dispersive materials. More information for these methods can be found in Ch. 8 of [PC3].

Chapter 2

Fabrication of woodpile structures

2.1 Introduction

In this chapter we are going to discuss the fabrication procedure of the three dimensional metallic woodpile structures according to the two-photon polymerization technique. Over the last few years, there has been an increased interest in corrugated metallic thin films and metal nanostructures. A lot of experiments have been realized on transmission enhancement through sub-wavelength arrays of holes [1], Raman scattering enhancement aimed at biosensing [2], and fabrication of metamaterials with permittivity and permeability simultaneously negative [3, 4]. Most of these photonic metamaterials [5, 6] have been structured by electron-beam lithography which is a two-dimensional (2D) fabrication technology. Very few experiments have been conducted on 3D micro- or nanofabrication, despite the fact that unique electromagnetic properties have been theoretically predicted [7-10]. The reason for this is in that the 3D fabrication of metallic, high resolution structures is challenging. To date, the most popular method for the fabrication of 3D metallic nanostructures is to prepare 3D dielectric structures using two-photon polymerization (2PP), and subsequently metalize these structures using electroless plating.

2PP is a direct laser writing technique that allows the construction of 3D structures with sub-micron resolution [11-13]. The major capability of 2PP lies in that it allows the fabrication of computer-designed, fully 3D structures with resolution beyond the diffraction limit. If the beam of an ultrafast laser is focused into the volume of a transparent photosensitive material, the polymerization process is initiated by non-linear absorption within the focal volume [14, 15]. Thus, by moving the laser focus in a 3 dimensional way, 3D structures can be made. To date several complex 3D devices have been fabricated [16-18], while resolution below 100 nm has been achieved [19]. So, by using photosensitive materials and applying laser powers that are only slightly above the polymerization threshold (via two-photon absorption), 3D structures with very high resolution can be achieved [20-22].

Metals are not transparent at the wavelengths that most femtosecond lasers operate (i.e. near infrared); therefore 2PP cannot be used directly for the fabrication of metallic 3D structures. A popular method for fabricating 3D metallic photonic materials is to fabricate dielectric structures using 2PP, and then metalize them to achieve the desired conductivity. The metalizing technique commonly used is electroless plating (EP). EP is cost-effective and the metal deposition can be done without using any electrical potential. This makes the technique very attractive for dielectric samples [23]. It allows homogeneous coating and even structures with arbitrary or complex shapes can be metalized [24].

To date, the materials used for the fabrication and subsequent metallization of 3D structures have been acrylate photopolymers and SU8. In this work, we employ hybrid organic-inorganic photostructurable materials, which incorporate metal binding groups, and which have been prepared using the sol-gel method. The sol-gel process, also known as chemical solution deposition, is a wet-chemical technique widely used in a variety of fields of materials science. Such method is used primarily for the fabrication of materials (typically metal oxides) starting from a chemical solution (or *sol*) that acts as the precursor for an integrated network (or *gel*) of either discrete particles or network polymers. It is a relatively new material technology, and is a useful tool for the fabrication of 3D structures using 2PP. The sol-gel also benefits from easy preperation, good mechanical stability, and good chemical and electrochemical inertness after photopolymerization. In combination with their high optical quality, sol-gel materials have found several applications in photonic devices such as photonic crystals and waveguides [25-29].

In this chapter we analyze the fabrication procedure that was followed throughout this work. Three basic stages were followed: First was the preperation of the materials via the sol-gel process, then the fabrication of the structures using 2PP and the final step was the metallization of them through electroless plating. Fig. 3 depicts schematically the processing flow for the fabrication of a metalized sol-gel material.

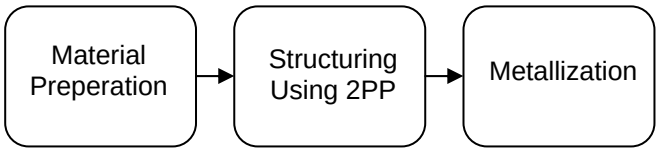

Figure 3: Processing flow of a photosensitive metalized sol-gel material.

2.2 Chemical reactions and methods

2.2.1 Sol-gel and metallization reactions

The first materials employed in 2PP were acrylic photopolymers and the negative photoresist SU8. Over the last few years, 2PP research has focused on photosensitive sol-gel hybrid materials [19] such as the commercially available ORMOCER® [30-32]. The sol-gel process is based on the phase transformation of a sol of metallic oxides or alkoxides precursors to form a wet gel. A photosensitive sol-gel process usually involves the catalytic hydrolysis of the sol-gel precursor(s) and the polycondensation of the hydrolyzed products and other sol-gel-active components present in the reaction medium to form a macromolecular hybrid network structure. The gel formed is subsequently reacted through photopolymerization to give a product similar to glass.

3D structure fabrication generally involves four steps: The first one is hydrolysis and condensation in which precursors or monomers such as metal oxides or metal alkoxides are mixed with water and then undergo hydrolysis and condensation to form a porous interconnected cluster structure. Either an acid such as HCl or a base like NH_3 can be employed as the catalyst.

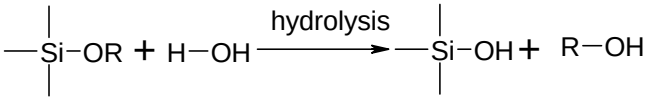

The second step is gelation, where the solvent is removed and a gel is formed by heating at low temperature. It is at this stage that solvents are removed and any significant volume loss occurs.

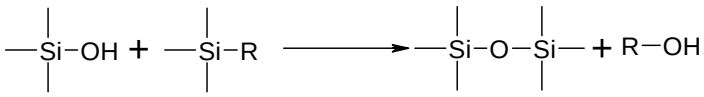

The third step of the process is the photopolymerization. Because of the presence of double bonds, and provided a photoinitiator is present in the gel, the photoinduced radicals will cause the polymerization of the unsaturated moieties only in the area the radicals are produced. At this step there is no material removal and no volume loss; the only reaction is the addition of the monomers to the active center. The last step is the development; the sample is immersed in an appropriate solvent and the area of the sample that is not photopolymerized is removed.

In this work, for the main backbone of the polymer we used a mixture of a silicon alkoxide with a zirconium alkoxide. By copolymerizing a silicon alkoxide with a zirconium alkoxide we can increase the material's mechanical stability and also modify its refractive index [33, 34]. The two main components of the copolymer used in sol-gel process are methacryloxypropyl trimethoxysilane (MAPTMS) and Zirconium *n*-propoxide (ZPO). Figures 4(a) and 4(c) demonstrate the hydrolization of the previous chemicals. The photoinitiator (PI) was 1% 4,4-bis(diethylamino) benzophenone (Fig. 4(d)). It is shown [35] that having 1% PI and 30% zirconium *n*-propoxide (compared to MAPTMS) the woodpiles had the best structural quality. However, ZPO concentration can not be increased above a critical point because there are instabilities that take place, like make the unpolymerized material insoluble in the developer. Lastly, dimethylaminoethyl methacrylate (DMAEMA, Fig. 4(b)) was added, which enables in the creation of metallic bonds, for the metallization procedure [36]. During gelation, the samples were heated and this resulted in the condensation of the hydroxy mineral moieties and the formation of the inorganic matrix (Fig. 4(e)).

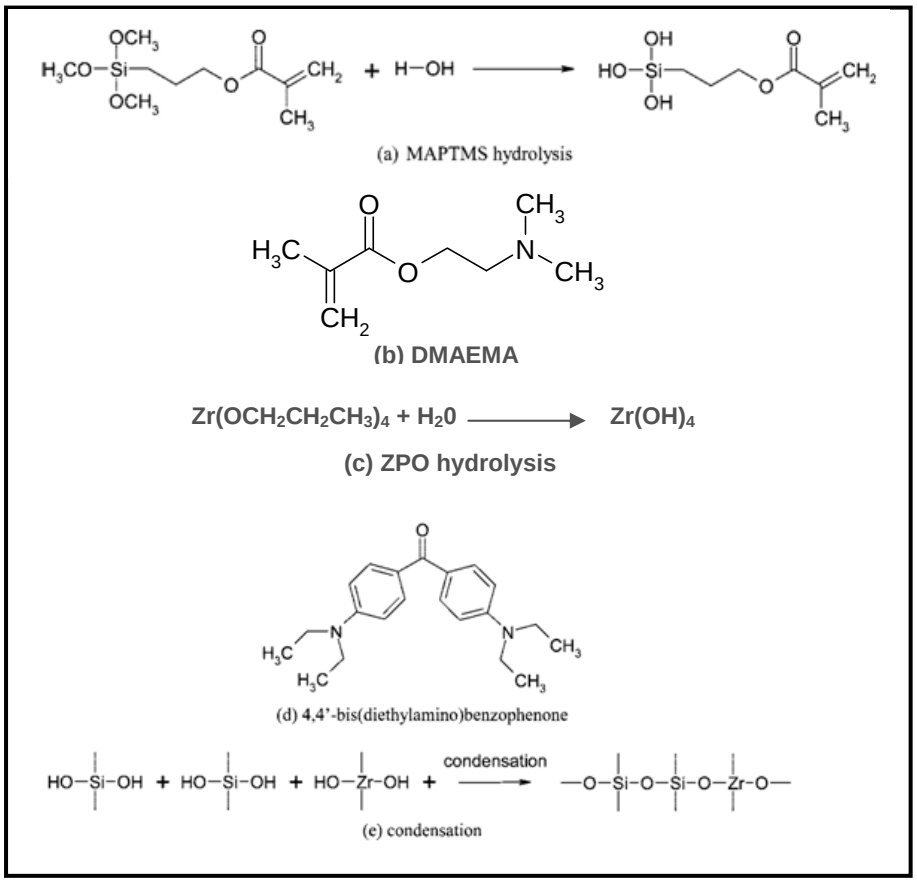

Figure 4: Chemical types of sol-gel process leading to the formation of the inorganic matrix.

As it is mentioned before, the metallization of our structures has been achieved through electroless plating (EP). The most common used metal particles are silver (Ag) and gold (Au). In this work, the deposited metal particles were silver. It is shown [37, 38], that the optical properties of silver-polymer composites depend strongly on silver layer thickness and nanoscale morphology. It is also known [39], that there is a shift to longer wavelengths as the metal nanoparticle diameter increases. However, the above statement is valid only when the metal layer thickness that surrounds the structure is larger than a critical value associated with the metal's skin depth. For silver the critical diameter is around 20 nm at 2-3 μm wavelength [40].

Unfortunately, the adhesion between the metal particles and the structured polymer is very weak [41]. Thus, a pretreatment is required in order to complete the EP successfully [42]. To increase silver nucleation and adhesion on the polymer structure, seeding and reduction steps are needed. In seeding process, a small concentration of silver particles is added in water. During this step, silver ions bind to the amine groups which remain open after polymerization. In reduction process, natriumborohydride is added in water and the silver ions are reduced to silver atoms. Finally, in electroless plating more metal particles are added (in higher concentration this time) along with other substances in order to stabilize the reaction (like arabic gum). By completing electroless plating, nanoparticles of silver are formed on the seeded area of the polymer and thus, the woodpiles are metalized (Fig. 5(b)).

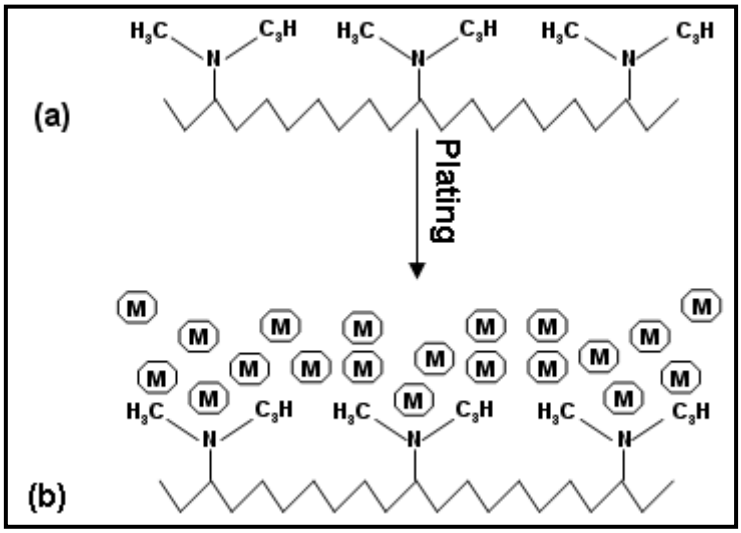

Figure 5: Metallization through electroless plating.

2.2.2 Material preperation methods

The main materials we used were MAPTMS (99%, M_n=248.35 gr/mol, d=1.045 gr/ml), DMAEMA (>99%, M_n=157.22 gr/mol, d=0.93 gr/ml) and ZPO (70% in 1-propanol, M_n=327.57 gr/mol, d=1.044 gr/ml). The molar ratios were 7:3 for MAPTMS/ZPO and 3:7 for DMAEMA/MAPTMS. The hydrolysis of MAPTMS was performed using HCl solution (0.1 M) at a 1:0.1 ratio. In a different bottle, we mixed DMAEMA and ZPO and let them stirred for 15 min. We then drop the hydrolyzed MAPTMS in the above mixture and thus we initiated the ZPO hydrolysis. The mixture was stirred for 30 min. Finally, we added the photoinitiator 4,4-bis(diethylamino) benzophenone, at a 1% w/w concentration to the final solution (MAPTMS + DMAEMA). The solution was filtered using 0.2 μm syringe filters. For gelation, we place a small drop of solution on a square glass and heated it at 50 ºC for 30 min, approximately.

In order to do the metallization procedure we, mainly, followed the steps of reference [43]. However, not all the chemicals were the same. Nanopure water (double distilled and heated) was used in all experiments. The materials that used were silver nitrate ($AgNO_3$, 99%), natriumborohydride ($NaBH_4$, 99%), glucose ($C_6H_{12}O_6$), ammonia water (NH_3, 25%) and arabic gum. For the seeding procedure we added 0.1699 gr of silver nitrate in 20 ml of nanopure water. We put the samples in the solution and let them for 38 hours. In the reduction process, we created a solution of natriumborohydride with nanopure water (2.505 gr of $NaBH_4$ in 15 ml). The time was ranged between 4 hours to 8 hours. For the plating procedure four solutions were made. The first solution had 3.96 gr of arabic gum in 12 ml nanopure water, the second 10.9534 gr of glucose in 32 ml nanopure water, the third 0.74 gr of ammonia in 12 ml nanopure water and the last one, 0.6794 gr of silver nitrate in 20 ml nanopure water. Then, we mixed the above solutions in a certain sequence. First we added silver nitrate in the arabic gum solution, then the glucose and after that, the ammonia. In the final solution we put the samples and let them for 6 min. The solution was covered with aluminum foil, so there was no interaction with light. Finally, the samples were rinsed in nanopure water and dried.

At this point it is important to mention that the samples that were metalized with the arabic gum as a stabilizer, proved not to be conductive (for more information read Section 3.2.1). As a result we modified electroless plating procedure according to Formanek's report [44]. Keeping the same masses and volumes as before, and completely removing the arabic gum from the procedure, aqueous ammonia was added dropwise to an aqueous silver nitrate until brown precipitates were formed and then dissolved. The electroless plating was initiated by adding the glucose solution to the silver nitrate solution. Because there was no stabilizer in the final solution the reaction was very rapid, thus the samples were left in the solution for 15-20 seconds only.

2.3 Fabrication using two-photon polymerization (2PP)

2.3.1 Basics of 2PP

A variety of materials used for 2PP are designed for conventional lithographic applications. There have been a lot of experiments using either negative or positive photoresists [11, 13, 45]. Negative photoresists are mainly used because the two-photon exposure results in the cross-linking of the polymer chains, making the exposed area insoluble to the solvent used to remove the unpolymerised material (developer). So, by using negative photoresists, there is a direct writing of the structures in the sample. Conversely, positive photoresists causes the photoresist polymeric chains to break and become soluble to the development solvent, so the reverse structure is written in the sample. Thus, by using negative photoresists together with the sol-gel technique we are able to develop photosensitive compounds [25].

By photopolymerization the liquid or gel monomers are converted into a solid polymer. As we mentioned before, the photoinitiator, PI, helps to start the reactions. By illuminating the PI with UV, visible or IR light active species are formed (active monomers). There are two kinds of PI depending on the nature of generated active species, either radicals or cations. The most commonly free radical PI is benzophenone and its derivatives, like the 4,4-bis(diethylamino) benzophenone we used in this work. Such PI have high quantum yield in the generation of the active moieties, high thermal stability and stability in darkness and are highly soluble in the polymerization medium. Using light, instead of heat, to drive the reaction yields some great advantages, such as the elimination of solvent, high reaction rates at room temperature, and spatial control of the polymerization [15].

The free radical polymerization procedure has at least three different kinds of reactions [30-32] that are summarized in Fig. 6. First step is initiation; the light decomposes the PI in the presence of monomer to form active species (Fig. 6(a)). Second step is propagation; the fragments of the initiator interact with a monomer and create the active adduct that is capable of being polymerized. After that, there are chain reactions and thus, more monomers are added creating macroradicals which have an active site at the chain-end (Fig. 4(b)). The last step is termination; the word termination means that the growth center becomes deactivated and thus, the polymerization stops. Termination usually involves the reaction between two polymer

chains and there are two possible mechanisms, combination (Fig. 4(c)) and disproportionation (Fig. 4(d)), leading to the formation of one or two polymer chains, respectively.

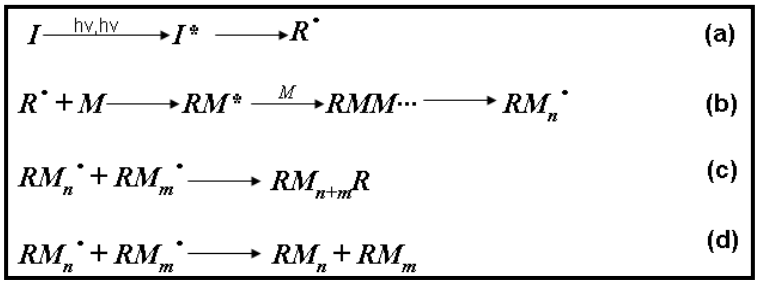

Figure 6: Two-photon polymerization process.

The heart of 2PP lies in a phenomenon called two-photon absorption (TPA). It describes the simultaneous absorption of two photons of identical or different frequencies in order to excite a molecule from one state, usually the ground state, to a higher energy electronic state. The energy difference between the involved lower and upper states of the molecule is equal to the sum of the energies of the two photons. Two-photon absorption is a second-order process, several orders of magnitude weaker than linear absorption. It differs from linear absorption in that the strength of absorption depends on the square of the light intensity, thus, it is a nonlinear optical process. So, when the laser is focused into a material (liquid or gel) the PI absorbs two photons and produces radicals. Because the material response is proportional to the square of the intensity, polymerization will take place only in the tightly focal point that the beam is focused leading us to very high spatial resolution [15].

TPA divides into two different types. One is sequential and the other simultaneous absorption. In sequential case, electrons are excited to a real intermediate state and, after that, a second photon is absorbed. This means that the intermediate state is a real energy level and the material absorbs at this frequency (Fig. 7(a)). In simultaneous absorption, which is the base of 2PP technique, there is no real intermediate state. This means that the structure will not absorb a photon that corresponds to that specific state and thus, the material is transparent. TPA happens only if a second photon arrives within the virtual state lifetime in order to excite the electron to the state S_2 [46] (Fig. 7(b)). This procedure demands the usage of very high intensities, which can only be created by a femtosecond laser.

It is worth mentioning that simultaneous absorption was predicted by Maria Göppert - Mayer in 1931 in her doctoral dissertation [47]. Her prediction was verified in 1961 (after the invention of laser in 1960) by Werner Kaiser when two-photon excited fluorescence was detected in a europium-doped crystal [48].

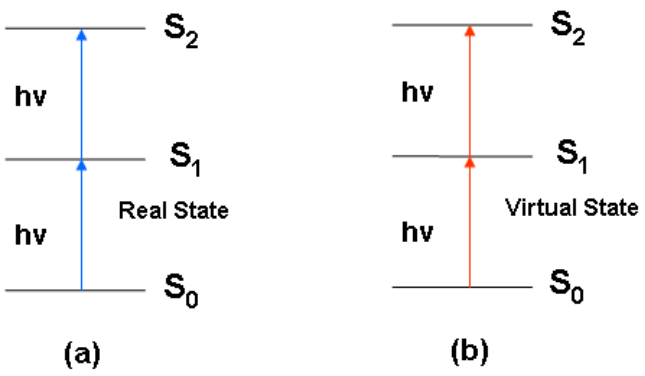

Figure 7: Band diagram of a real and virtual state. In sequential case the intermediate state is a real energy level (a), while in simultaneous it is virtual (b).

A reasonable question that generates is what is the highest resolution that can be achieved. Theory predicts a limit in the resolution that can be achieved by a focused laser beam. This limit is called Abbe's diffraction limit. Ernst Abbe was born in Germany in 1840. He spent most of his time in Jena where he developed a mathematical description for the resolution limit of the microscope. The optical resolution d is defined as the minimum distance of two structural elements to be imaged as two objects instead of one. Abbe found the equation below [49]:

$$d = \frac{\lambda}{2\,(N.A.)} \tag{13}$$

where λ is the wavelength of light and *N.A.* is the numerical aperture of the objective, defined as the sine of the half aperture angle multiplied by the refractive index of the medium filling the space between the cover glass and the front lens (i.e. $N.A. = n \cdot \sin(\theta)$).

After this discovery, there has been an increasing interest of the scientific community to decrease the wavelengths in a number of experimental techniques, like atomic force microscopy (AFM) [50-54] and near-field scanning optical microscopy (NSOM) [55-57]. However, these techniques allow 2D patterning, only. In order to produce 3D structures, with photopolymerized voxels smaller than the diffraction limit, materials with very well defined photopolymerization threshold are needed.

As we mentioned before, the laser light decomposes the PI and so radicals are produced. These radicals are quenched, mainly, by oxygen. Generally, quenching is a bad effect for photopolymerization, because the radical becomes inactive after quenching and thus photopolymerization is difficult to initiate. However, in 2PP quenching can be used to bypass the diffraction limit and creates materials with very good resolution. This is possible by modifying the light intensity that passes through the medium, in a way that the light produced radicals exceed the quenchers and initiate 2PP only in a small volume where the energy of the beam is higher than the threshold energy (for more information read [PC7]).

2.3.2 Experimental setup

Fig. 8 depicts the experimental setup used for the fabrication of 3D micro-structures by 2PP. The laser source is a Ti:sapphire femtosecond oscillator, operating at 800 nm, with integrated dispersive mirrors. The pulse length of the laser is less than 20 fs while the repetition rate is 75 MHz (Femtolasers Fusion). The maximum output power of the oscillator is 450 mW, however, the output power that used in the experiments of this report varied from 310 mW to 380 mW.

The laser beam passes through an attenuator (Altechna), in order to reduce its intensity without appreciably distorting its waveform, and with the correct alignment of mirrors, reaches the *x-y* galvanometric mirror digital scanner (Scanlabs Hurryscan II) controlled by SAMLight (SCAPS) software. In the beam's path a shutter (Uniblitz) is placed in order to forbid or allow the light to reach the samples. The scanner is adapted to accommodate a high numerical aperture focusing microscope objective lens (100x, N.A. = 1.4, Zeiss, Plan Apochromat). Because the numerical aperture of the objective is higher than 1, immersion oil is used for index matching. Movement on the x, y, z axis is carried out with a three-axis linear encoder stage. The control of the stages, the attenuator and the shutter is achieved via a National Instruments LabVIEW program. During photopolymerization the refractive index of the copolymer changes and the structures becomes visible, that is why, a CCD camera is mounted behind a dichroic mirror for online monitoring of 2PP process. It worth noting that, during this work, a new fully 3-dimensional stage was purchased (Scanlabs Hurryscan 10) replacing the galvanometric mirror digital scanner. Additionally, the programs that were responsible for the control of the fabrication procedure were replaced by 3D Poli software made by Vytautas Purlys.

All the structures were fabricated layer-by-layer with the last layer on the surface of the glass coverslip, which means that the fabrication was started from the top layer and moved negatively to the bottom. This was done in order to avoid the laser beam to pass through an already polymerized layer a second time. After the building process was completed, the structures were developed first in 4-mehyl-2-pentanone, after in 1-propanol, and lastly in dimethyl sulfoxide solutions (10 min in each one).

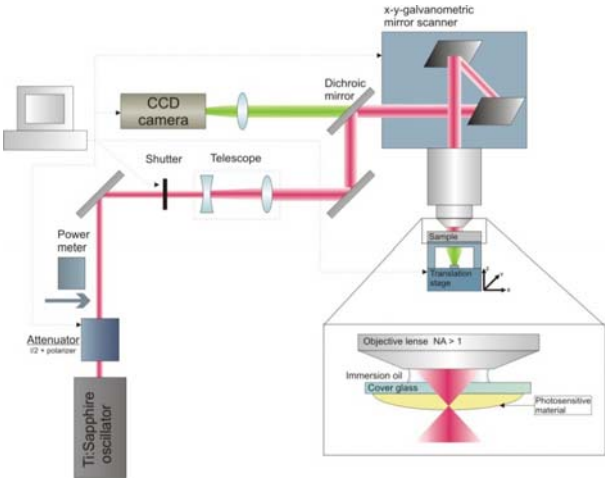

Figure 8: A common experimental setup for the 2PP. The image shows a fs laser, a galvanometric mirror scanner, moving stages, directional and focusing optics and a monitoring camera.

Chapter 3

Characterization of woodpile structures

3.1 Introduction

To date there have been numerous experimental work on the optical characterization of woodpile photonic crystals [1-4]. Both fct [5] and fcc [6] geometries have been examined, while complete photonic bandgap with a ratio of 6.9% (gap-to-midgap) near the telecommunication regime (~1.55 μm) has been achieved recently [7].

In this chapter we are going to discuss the characterization results of our metalized fcc woodpile structures. The first section (3.2.1) investigates the resistance of the samples in order to find out if the metalized woodpiles have high or low conductivity. The second section (3.2.2) depicts some structure images for two different periodicities, namely 600 nm and 900 nm, and analyzes the influence of various experimental parameters (like the intensity power during fabrication, the metallization time during pretreatment and so on) on the structural quality of the woodpiles. This analysis helps us to find the best experimental conditions that allow as to fabricate high resolution structures. Finally, the last section (3.2.3) demonstrates some experimental transmission results of the woodpiles and compares them with the respective theory.

3.2 Characterization results

3.2.1 Measurement of resistance

The first part of the characterization process was to examine the resistance of the structures. As we have already discussed in Section 2.2.2, the structures were metalized with silver. Thus, we expect the samples to have a resistance of only a few Ohms in order to be highly conductive. Additionally, to have metallic behaviour, the dependence of intensity and voltage should be linear (so that the Ohm's law keeps). The equipment used for analyzing the current-voltage (I-V) characteristics of the metalized structures was a Tektronix 370 curve tracer. Through needles, the voltage was applied and the resistance was calculated by the slope of the line of the I-V curve.

At this point it is important to mention two problems that came up during this procedure. The measurement device can not be used for structures of area smaller than 150^2 μm^2 due to the quite large lateral size of the needles. Taking into consideration that the average time to fabricate a woodpile of 40^2 μm^2 is around 5 hours, it will be very time consuming to reach the size of 150^2 μm^2. Additionally, if we do manage to achieve the desired structure area, the needles will destroy, locally, the structures when placed on them. To overcome these obstacles we created solid bulk boxes of the same material as of our structures, and then we metalized them following exactly the same steps as in the woodpile metallization. During the measurements all the samples that were metalized with arabic gum as a stabilizer were proved to have a non-Ohmic behaviour while the resistance was high. The experimental results, for the samples that were metalized without the presence of stabilizer, are demonstrated in Fig. 9.

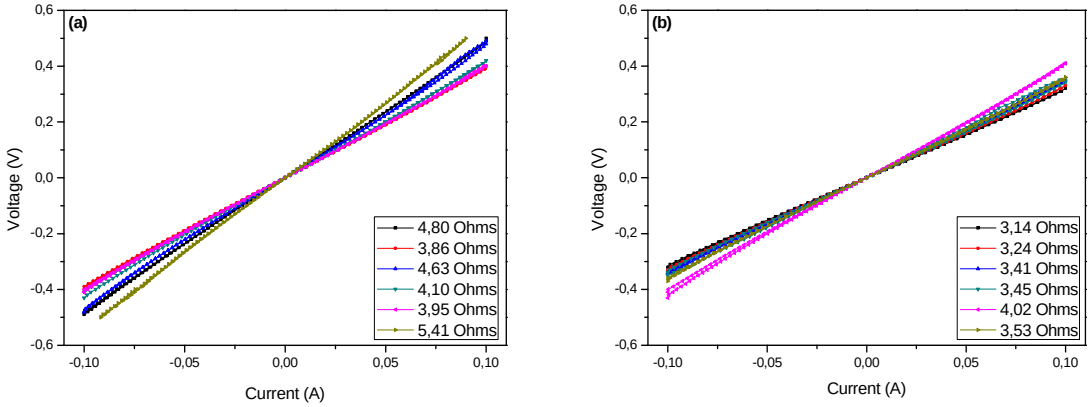

Figure 9: Current-voltage diagrams for 12, in total, samples (metalized without the presence of stabilizer). The legends show the calculated resistance for each sample. Both (a) and (b) images show Ohmic behavior and low resistance.

The area of those samples ranged from 150^2 to 200^2 μm^2 while the height remained fixed, at 10 μm approximately. However, no significant change occurred in calculated resistance so; the resistance was independent of the area (at least on that scale). We have to note here that all the measurements were taken with the needles to be on the opposite corners of each square. The graphs shown in Fig. 9 are linear fits of the plots acquired by the curve tracer at low currents. From those graphs it is clear that all the samples showed Ohmic behaviour while the average resistance was 4.46 ± 0.49 Ohms for the samples of Fig. 9(a) and 3.46 ± 0.21 Ohms for those of Fig. 9(b). The same procedure was repeated two more times with, approximately, the same results (not shown here). Although the previous technique can not calculate the resistivity, the conductivity of the samples should be rather high since all the samples showed very low resistance. Thus the woodpiles should have about the same conductivity as in the case of pure silver (~ 10^7 Ohms^{-1} m^{-1}).

3.2.2 Resolution analysis at different experimental parameters

In this section we are going to demonstrate some images of the woodpile structures that were fabricated, before and after the metallization process. As we have mentioned in the introduction of this chapter, the woodpiles that were fabricated had 600 nm and 900 nm period. Since we investigate the fcc geometry the unit cell height was c_{600} = 848.5 nm and c_{900} = 1272.8 nm, respectively. Thus, the distance between two adjacent layers (from center-to-center) was $\alpha_{600} = c_{600}/4$ = 212.1 nm, and $\alpha_{900} = c_{900}/4$ = 318.2 nm. All the 900 nm periodicity structures were fabricated with the x-y galvanometric scanner while the decrease in periodicity was achieved using a 3D movable stage. We should also note that the images were taken either with Scanning Electron Microscope (SEM) or Field Emission (FE) analysis, so, from now on, all the images will have the SEM or FE acronyms in the explanation text under the photos. Figure 10 shows a typical dielectric woodpile structure.

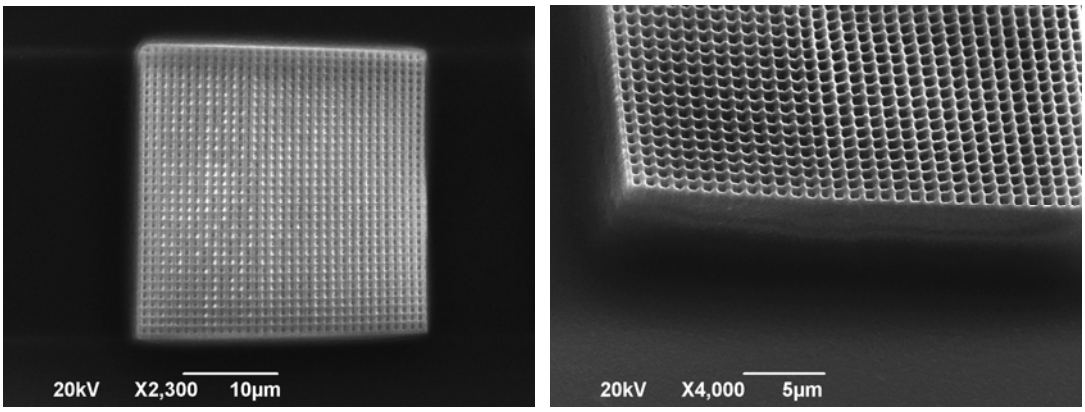

(a) (b)

Figure 10: (SEM) Typical images of a dielectric woodpile structure (900 nm period). (a) shows a top view and (b) a 45º side view of the structure.

The area of the structure is 30^2 μm^2 and the height 7.5 μm approximately. This means that there are 6 unit cells fabricated along the height axis. During each woodpile fabrication, the laser was programmed to structure some layers inside the substrate (which in our case was glass) in order to be sure that the structure will not wash away during the development. In Fig. 10(b), the layers which are under the topmost one are not visible. That is because the laser beam polymerized the perimeter of each layer, apart from the structure, in order to increase the stability of the layers. However, this option has been removed in order to examine the other layers too.

- ***Role of the incident beam intensity***

An interesting case is to examine the dependence of the resolution (i.e. the width of rods) on the intensity of the incident beam. This is a critical step in this work, because the primary goal is to maximize the resolution of the structures; that is to

make rods as thin as possible. Fig. 11 depicts four dielectric woodpile structures that were fabricated at different intensities.

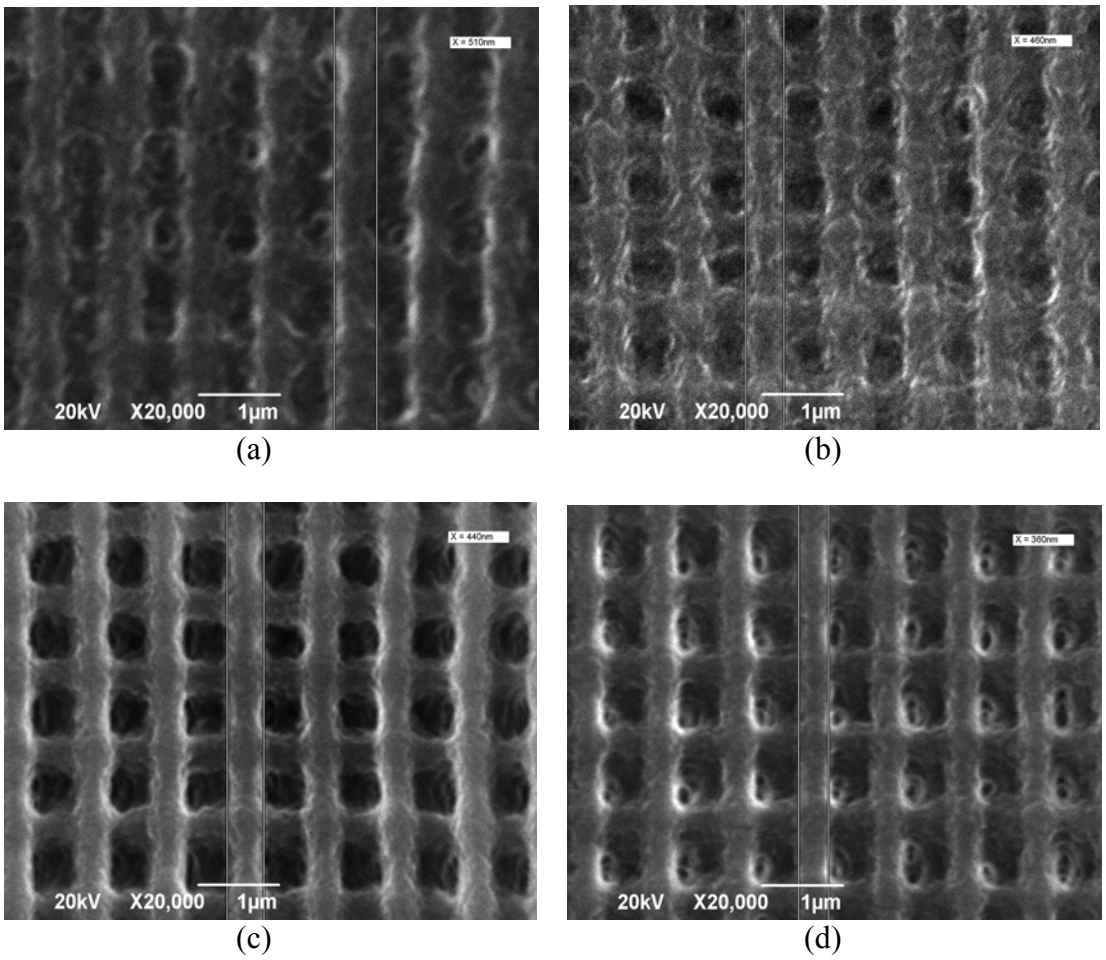

Figure 11: (SEM) Dielectric woodpile structures obtained at different laser beam intensities (900 nm period). The average width of each rod is 510 nm at 3.15 mW (a), 460 nm at 2.77 mW (b), 440 nm at 2.55 mW (c), and 360 nm at 2.20 mW (d).

The pictures presented in Fig. 11 show that the resolution increases when intensity lowers. As we move from 3.15 mW (Fig. 11(a)) to 2.20 mW (Fig. 11(d)) the mean width of the rods decreases from 510 nm to 360 nm. As the intensity increases the average focal polymerization spot increases too, explaining thus the change in the width of the rods. The above observation is in agreement with earlier results both theoretical [8] and experimental [9]. The same behavior was experienced on the 600 nm periodicity structures.

So, the next step in this work is to find the minimum intensity (threshold intensity) that is enough to fabricate structures of a given periodicity. Since, threshold intensity is not the same for metalized and non-metalized structures (the structure that has been fabricated by 2PP may be washed out or ruined after metallization) threshold intensity will be measured after metallization.

Another important topic, related also with the laser intensity, is shrinkage. It should be mentioned that most of the volume loss takes place during the gelation

process. However, there is also shrinkage due to 2PP. This shrinkage is non-uniform and it is difficult to avoid it when polymerized microstructures are attached to substrates. If the intensity is well above the threshold limit, the shrinkage is almost absent; but in the case of high structural resolution which demands intensity values near the threshold one, the phenomenon is rather intense [10]. It is also shown, in reference [36] of chapter 2, that the linear strain of a zirconium-based sol-gel composite (like the one in this work) increases exponentially by decreasing the average laser power. Figure 12 demonstrates two woodpile structures with a characteristic deformation shape due to shrinkage.

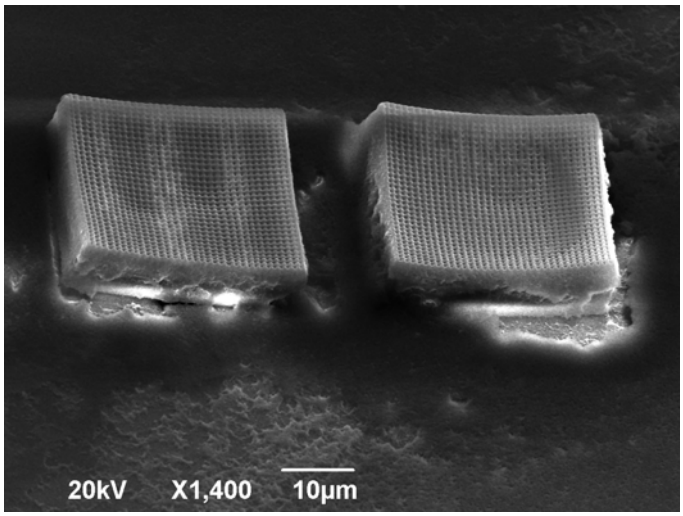

Figure 12: (SEM) Two woodpile structures (900 nm period) with a characteristic deformation shape (a curve at the center of each structure) due to shrinkage.

- ***Role of the laser beam alignment***

Next step was to examine the woodpile images that were taken after the metallization procedure. The geometrical characteristics were the same as before. However, before we continue the analysis, it is important to discuss a phenomenon that has to do with the correct calibration of the laser beam. Fig. 13(a) shows six fabricated and metalized structures. The laser intensity is 3 mW for structure a and, gradually, goes down to 2.37 mW for f. It is clear that, as we move to lower intensities, the structures start to be destroyed. However, as we are going to show in the next pages, all the intensities higher than 2 mW are enough for a stable fabrication for both periodicities. Furthermore, if we examine structure f (Fig. 11(b)), we will see that the polymer chains are stable and well structured. So, what causes this collapse, if it is not the intensity? The phenomenon has to do with the correct alignment of the laser beam and the sample's substrate (glass). If the beam is not centered very well on the sample, the intensity will be inhomogeneous and thus, the error will continuously increase as we move away from that point. Additionally, the substrate where the sample (hard gel) is on must be perpendicular to the laser beam at all times during fabrication. Even a small tilt from this orientation can cause big fabrication errors since part of the structures could be fabricated inside the glass, explaining the

characteristic behavior of Fig. 13(a). For these reasons, structure a is well fabricated, but, as we move to structure f the upper left corner of the woodpiles starts to collapse.

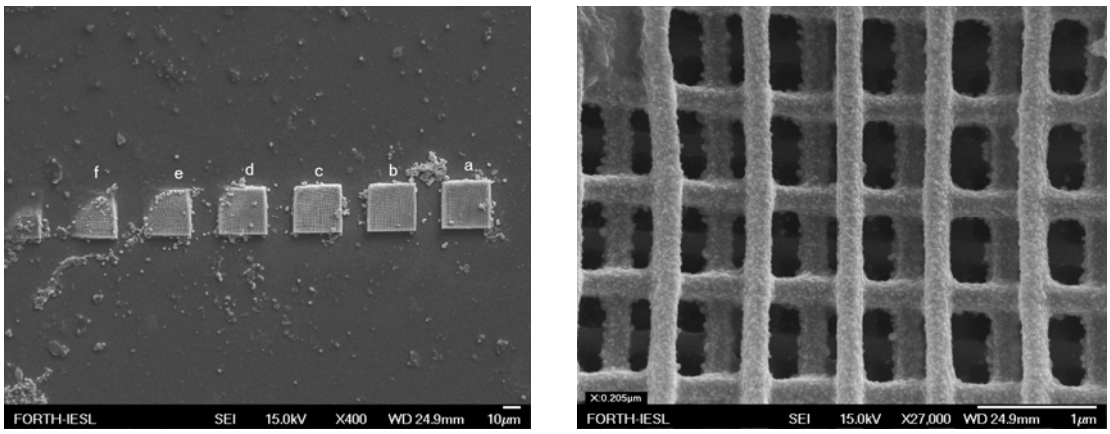

(a) (b)

Figure 13: (FE) (a) Top-view of 6 woodpile structures obtained at different laser beam intensities. The laser beam is not well centred that is why the top left corner of the structures start to collapse as we move from a to f. (b) A magnified top-view of structure f. From the image it is clear that the intensity is enough for fabrication.

- ***Role of the reduction time and stabilizer***

Since we clarified the issue of the correct alignment, we continued the analysis by examining the shape and the metallization of the samples. Fig. 14 demonstrates a typical metalized woodpile structure (900 nm period) from different viewpoints. From the images we can make the following observations: a) In Fig. 14(b) we have drawn horizontal lines that follow a layer of the structure. It is clear that as we move to the corners the rods start to deviate from the lines. This phenomenon is due to shrinkage and has already been discussed. However, the shrinkage is small, so there is little distortion. b) There is a formation of big silver particles on and around the structures (Fig. 14(a)-(c)). This means that the time during the reduction process was higher than it should be.

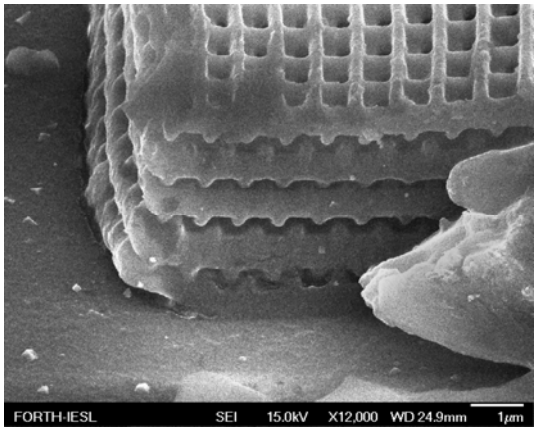

(a)

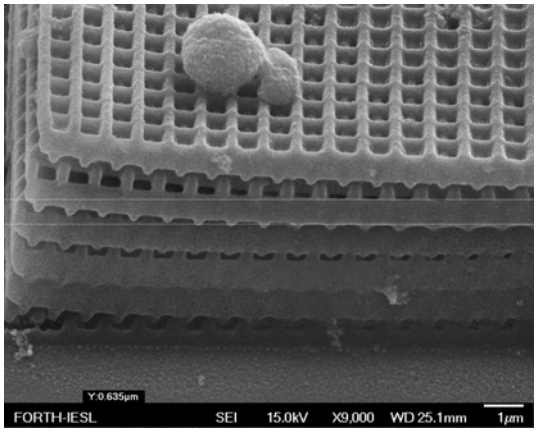

(b)

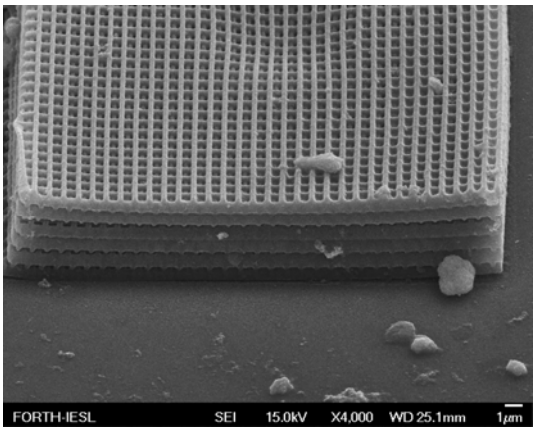

(c)

Figure 14: (FE) Woodpile structures (900 nm period) after metallization. Corner (a) and side (b), (c) views of structure. The layers are ramped due to shrinkage while the silver particles that are formed on and around the structures mean that the reduction time was high.

In order to find the appropriate reduction time, the reduction time for various samples was examined. Fig. 15(b)-(d) depicts three woodpile structures at different reduction times. The times are 4, 6 and 8 hours for structures (b), (c) and (d) respectively, while the periodicity is fixed at 900 nm. The electroless plating time was the same for all structures (~6 min). It is clear that when the reduction time increases there is, also, a significant increase of the average diameter of the accumulated silver particles. Although this accumulation is part of the metallization procedure (i.e. the metal coating is achieved through the deposition of the silver particles), the very rapid accumulation of silver should be avoided. From the images, one can see that there is a critical time (between 6 and 8 hours) beyond which the silver deposition is so rapid that it forms huge particles of silver (Fig. 15(d)). The average diameter was measured to be around 20 nm for structure (b), 30 nm for (c) and 180 nm for (d). The periodicity of structure (d) is destroyed due to the formation of very big silver particles which means that the reduction time was well above the proper one. Even structure (c) which is homogenously silver-deposited has quite big particles. This leads us to the conclusion that lower reduction times are needed (possibly around 4 hours) in order to achieve the optimum resolution. However, the above results are valid only in the case where the stabilizer (arabic gum) was present during the electroless plating. Fig. 15(a)

shows a 600 nm periodicity woodpile, metalized without the stabilizer in order to be highly conductive. The reduction time was only 30 min, while the electroless plating time around 20 sec. Despite the low times, it is clear that the metallization is so rapid that metal particles of a diameter of 50 nm approximately are formed around the rods, thus it is quite difficult to control the thickness of silver deposition with the absence of stabilizer. However, this was the preferred method in our work since it has allowed us to make highly conductive structures (see Section 3.2.1 for more information).

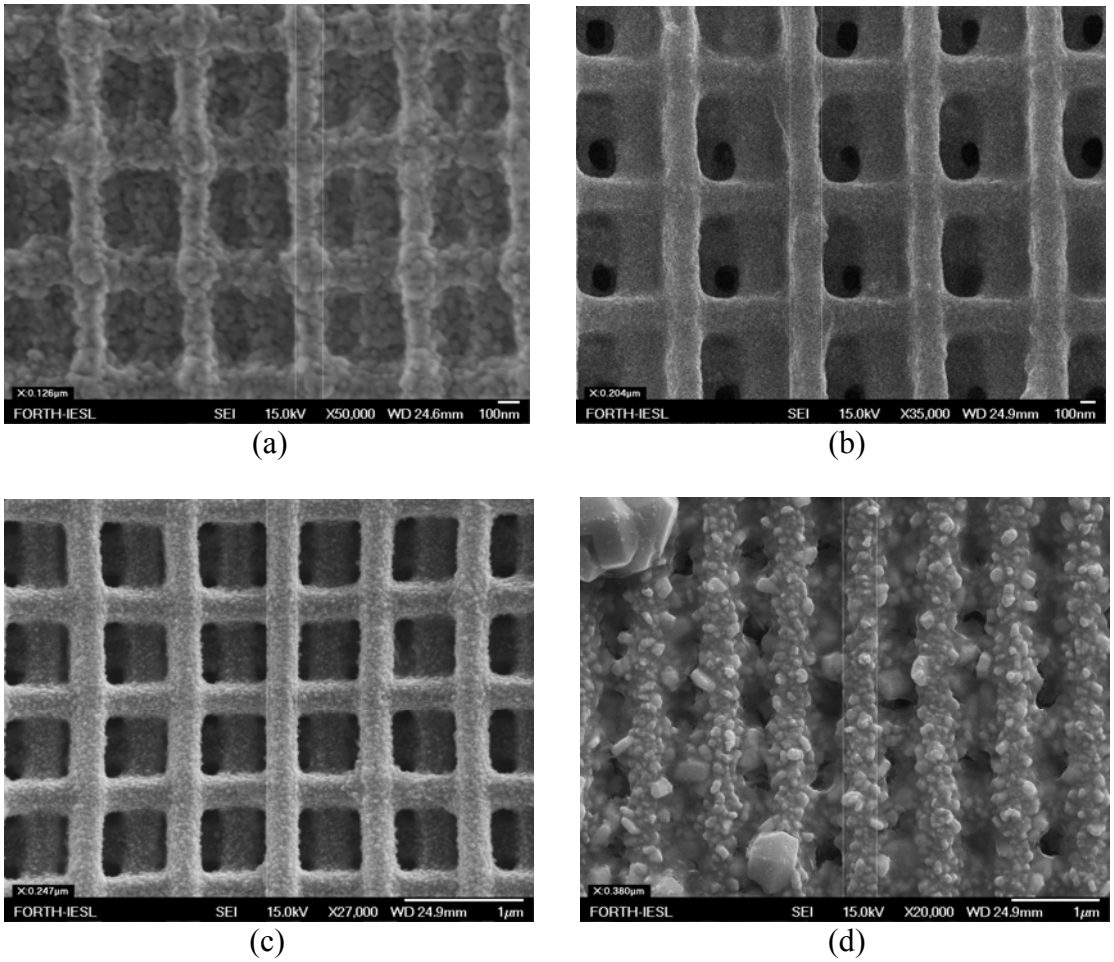

Figure 15: (FE) Top-view of four different woodpile structures obtained at different reduction and plating times. Fig. (a) was metalized without stabilizer, while (b)-(c) with. The reduction time for structures (b), (c) and (d) was 4, 6 and 8 hours respectively (plating time was fixed at ~6 min); while for structure (a) it was 30 min (plating time ~20 sec).

- ***Threshold intensity***

Finally, the threshold intensities were investigated and measured for the two different periodicities. Fig. 16(a)-(b) depict two 900 nm periodicity woodpiles fabricated at 2.05 mW (a) and 1.96 mW (b), while the next two images demonstrate two 600 nm periodicity woodpiles fabricated at 1.90 mW (c) and 1.82 mW (d). Apart from the accumulated silver particles mainly at the edges, the rods of structures (a)

and (c) are stable and not broken. On the contrary, structures (b) and (d) are unstable with lot of distorted and broken regions (especially at the edges). This means that the threshold intensity should be around 2 mW and 1.85 mW for the 900 nm and 600 nm periodicities, respectively. At this point we should remind that the above threshold intensities are valid only for the discussed geometrical characteristics and molar ratios (7:3 for MAPTMS/ZPO and 3:7 for DMAEMA/MAPTMS).

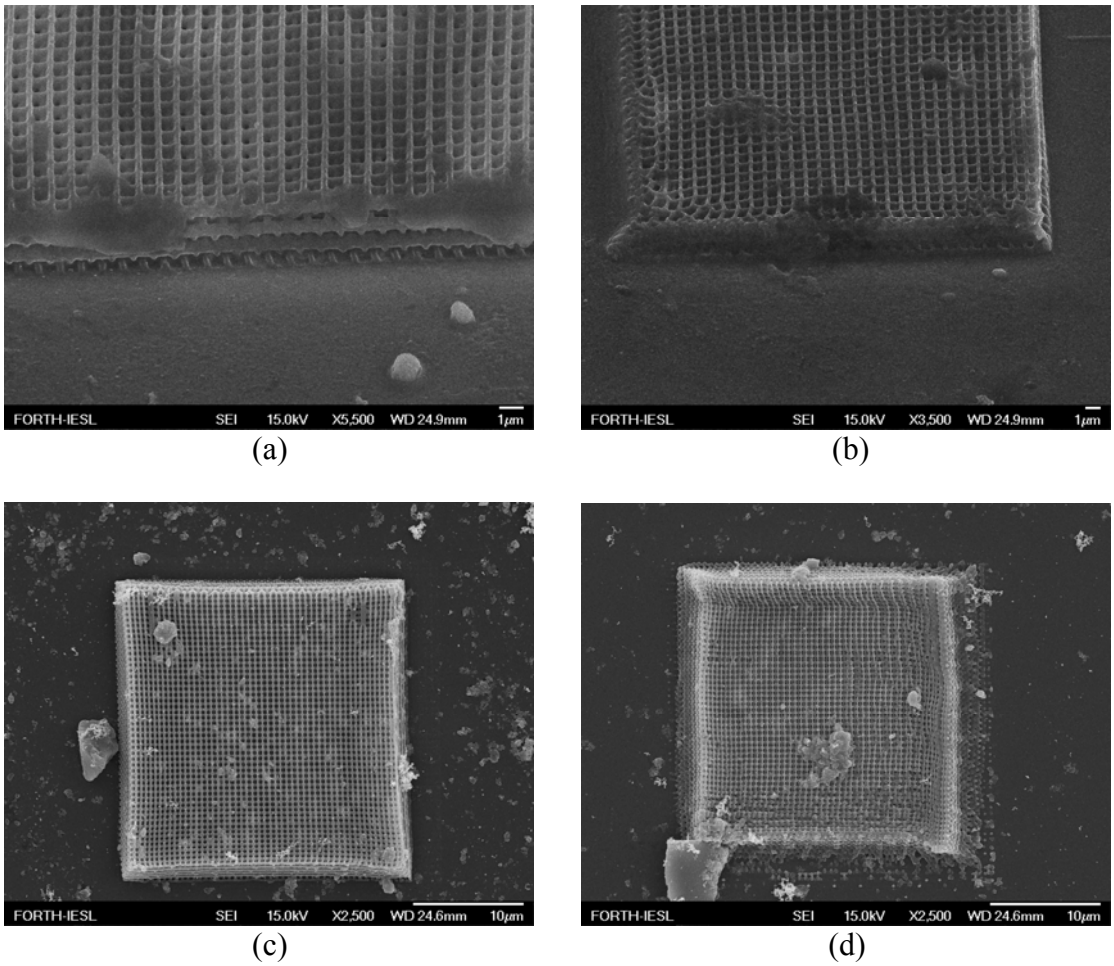

Figure 16: (FE) Finding the threshold intensities for the 600 nm and 900 nm periodicity structures. (a), (b) Side view of two 900 nm periodicity woodpile structures. (c), (d) Top-view of two 600 nm periodicity woodpile structures. The fabrication intensities were 2.05 mW (a), 1.96 mW (b), 1.90 mW (c), and 1.82 mW (d). Structures (a) and (c) are stable and well-formed, while (b) and (d) are distorted and broken. Thus, threshold intensity is around 2 mW and 1.85 mW for the 900 nm and 600 nm periodicities respectively.

It is also interesting to take a closer look at the 600 nm periodicity structures (Fig. 16(c) and (d)) in order to examine the resolution that has been achieved at the lowest intensities. The related images show that the corresponding average thickness for these structures is 103 nm for Fig. 16(c) and 82 nm for Fig. 16(d). If we consider the fact that during metallization the rod thickness increases, the resolution is very high.

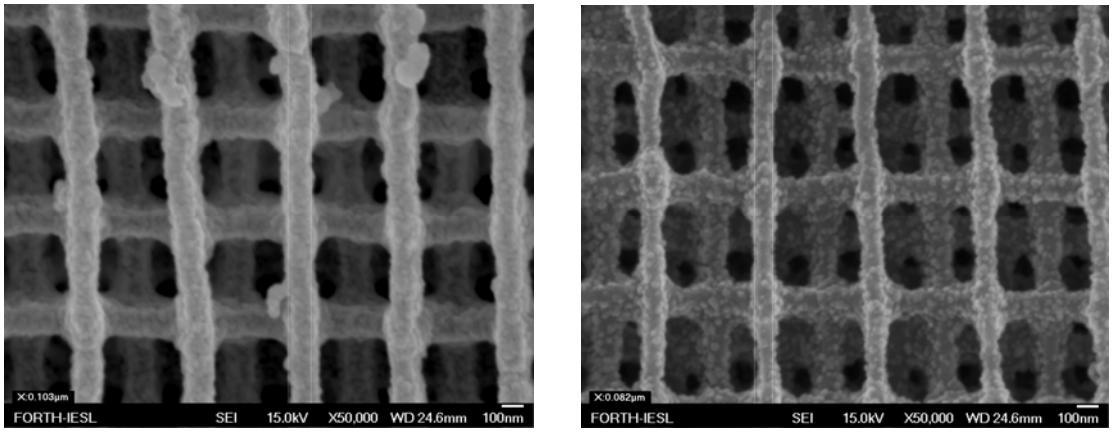

(a) (b)

Figure 17: (FE) (a) (b) Resolution analysis for the images of Fig. 16(c) and (d), respectively. The average resolution of (a) is about 100 nm, while just under threshold intensity, resolution of 80 nm, approximately, has been achieved (b).

Summarizing, in this section we examined the influence of various experimental parameters (laser intensity and alignment, reduction time etc.) on the geometry and the quality of the metallic woodpile structures. Thus, we identified for our structures the threshold intensities (2 mW and 1.85 mW for the 900 nm and 600 nm periodicities respectively) and the optimum times for the reduction and electroless plating procedures with (reduction time ~ 4 hours, electroless plating time ~ 10 min) and without (reduction time ~ 30 min, electroless plating time ~ 20 sec) the stabilizer. These results lead us to very high resolution structures (~100 nm).

3.2.3 Transmission analysis

In this part, the EM wave transmission through our structures was measured and compared with the corresponding theory. The scheme of Fig. 18 demonstrates the experimental setup for the transmission measurements. Synoptically the steps are the following: A source creates white light (pump center at 1064 nm) and emits it through an optical fiber (100 μm diameter). The beam, with the correct alignment of mirrors and lenses, is focused on the sample. The diameter of the focused beam in the sample is 24 μm, approximately. The transmitted light focuses in the optical fiber (100 μm diameter) of the optical spectrum analyzer which is connected with a computer that shows the transmission graphs. We should note that the spectrometer can measure a frequency range from 300 THz to 750 THz (1000 nm-400 nm). Due to this range limitation, the 900 nm periodicity structures could not be characterized since the first transmission band starts at a frequency of 200 THz (~1500 nm) approximately.

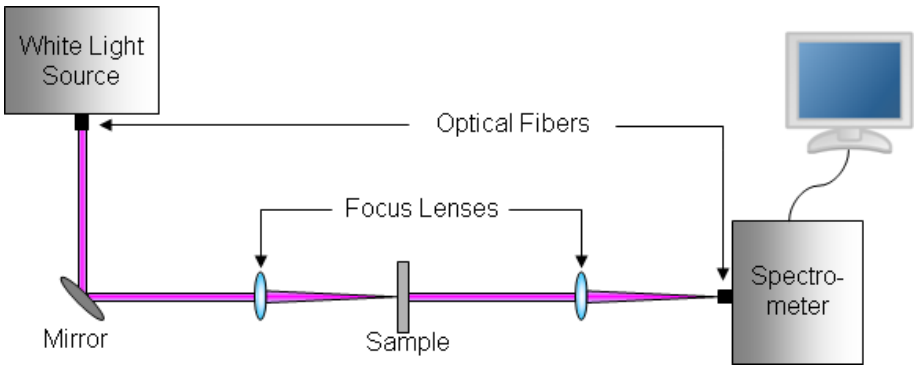

Figure 18: Scheme of the experimental arrangement for the transmission measurements.

Concerning the theoretical analysis, as we mentioned in the last page of Ch. 1, there are various numerical methods for the calculation of the bandgaps of a structure. For our woodpile structures, the most preferable method was FDTD, since it can measure the transmission properties over a wide frequency range in a single calculation. The program we used for the simulations was CST Microwave studio®. Figure 19(a) depicts a perspective view of the simulated woodpile structure. The structure contains 4 unit cells along the propagation direction (z-axis) while periodic boundary conditions are employed along the other directions. Each cell has 4 elliptical rods that intersect with their neighbors in order to be as close to the experimental case. The two red squares shown in Fig. 19(a) correspond to the source, which creates Gaussian pulses, and the analyzer, that collects the transmitted light. The material of the rod is silver that follows the Drude model we described in the last section of Ch. 1. Of course in reality, the rods are made by a polymer surrounded by silver rather than by bulk silver. However, at the THz frequencies the silver skin depth is only a few nanometers so that it is always lower than the thickness of the silver deposited on the rods. Thus, light does not interact with the dielectric material but only with the silver particles.

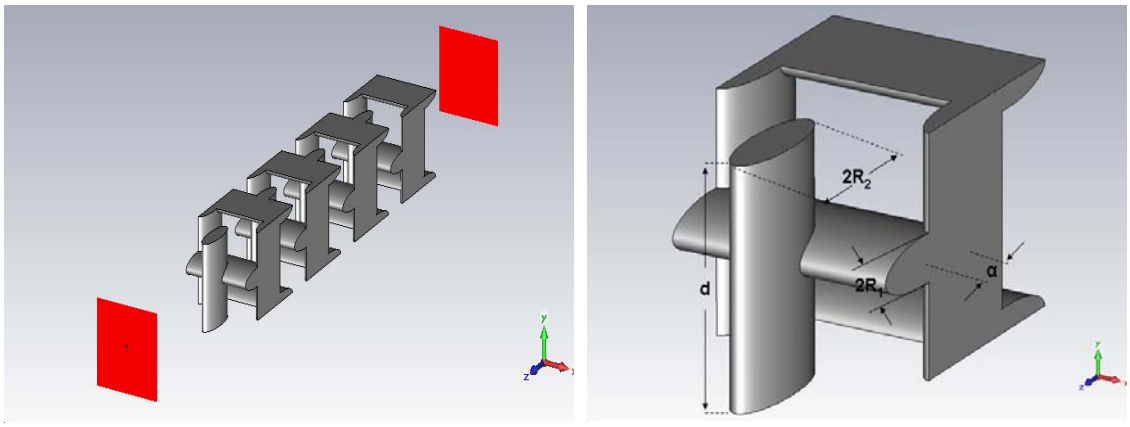

(a) (b)

Figure 19: (a) Simulated silver woodpile structure that contains 4 unit cells along propagation direction. The red squares represent the source and the analyzer. (b) Closed-up view of 1 unit cell showing the fundamental geometric parameters used for the simulation.

There were four basic geometrical structure parameters that could be modified during simulations: The rod distance, α, which by definition is the distance, from center-to-center, of two adjacent rods along z-axis (see Fig. 19(b)), the period (lattice constant), d, of the structure, and the small (R_1) and big (R_2) radius of the elliptical cylinders. To compare with experimental data we chose periodicity 600 nm. For the periodicity of 600 nm the lattice constant was fixed at 212 nm, so that $c_{600}/d = 4\alpha_{600}/d = \sqrt{2}$ (where c_{600}, as we mentioned in Section 3.2.2, is the unit cell height along z-axis). By modifying the radii of the cylinders the filling ratio of the unit cell was changed.

In order to find the appropriate radii for the modeling as to approximate the experimental structures, we took some field emission (FE) images of a chosen woodpile of d=600 nm (the area of the structure was 40^2 μm^2) which are shown in Fig. 20. Fig. 20(a) and (b) show that the structure is clean since it does not have any big metal particles on or around. From Fig. 20(c) and (d) we see that the average small diameter is around 120-130 nm (R_1 = 60-65 nm) while the big one is 310-320 nm (R_2 = 155-160 nm) approximately. At this point we should note that it is frequent some layers at the bottom of the structure to collapse due to shrinkage. That is why some of the bottom layers of Fig. 20(e) seem to have twice the thickness of the top ones. The same image (Fig. 20(e)) also shows that the height of the structure is 4-5 unit cells. Lastly, From Fig. 20(f) we observe that the dimension of the metal particles is around 40-50 nm, which is greater than the skin depth of light in the THz region.

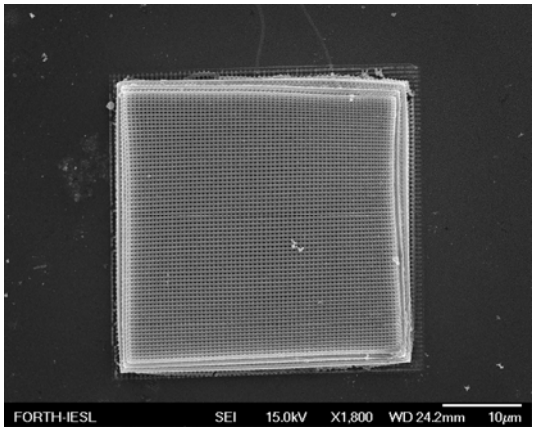

(a)

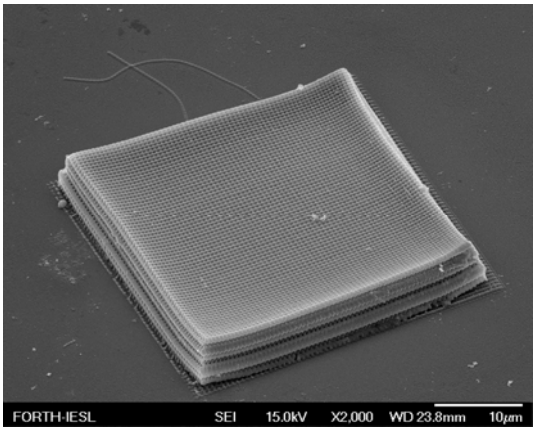

(b)

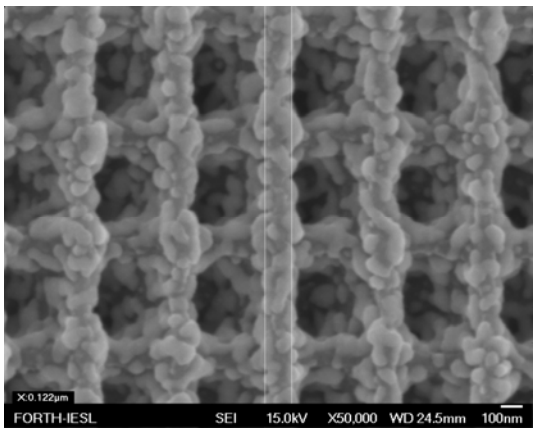

(c)

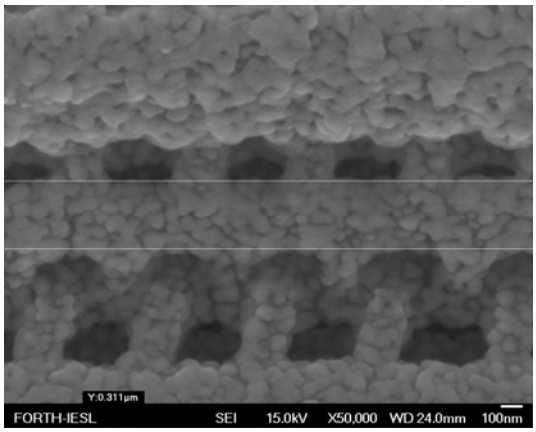

(d)

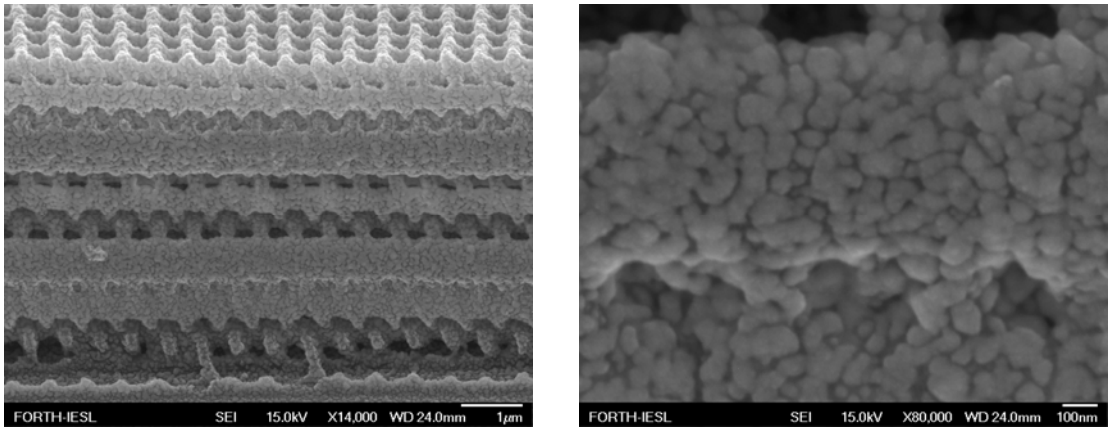

(e) (f)

Figure 20: (FE) (a) (b) Top and diagonal view of a structure of 600 nm period. (c) (d) Measurement of the small (~125 nm) and the big (~310 nm) diameter, respectively. (e) Some of the bottom layers have been merged due to shrinkage, while the total height of the structure is 4-5 unit cells. (f) Close view showing that the average dimension of the silver particles is around 40-50 nm, greater than the skin depth.

By changing the filling ratio (i.e. R_1 and $R_2(\approx 3R_1)$) of the unit cell and keeping α and d fixed, multiple simulations were achieved. We should note that during all simulations there were 4 unit cells along **k**-axis (the same number as in the experimental structures). The space between the silver rods was considered to be vacuum. The results that were closer to the experimental ones were for R_1 = 60 nm and R_2 = 180 nm and are demonstrated in Fig. 21(a).

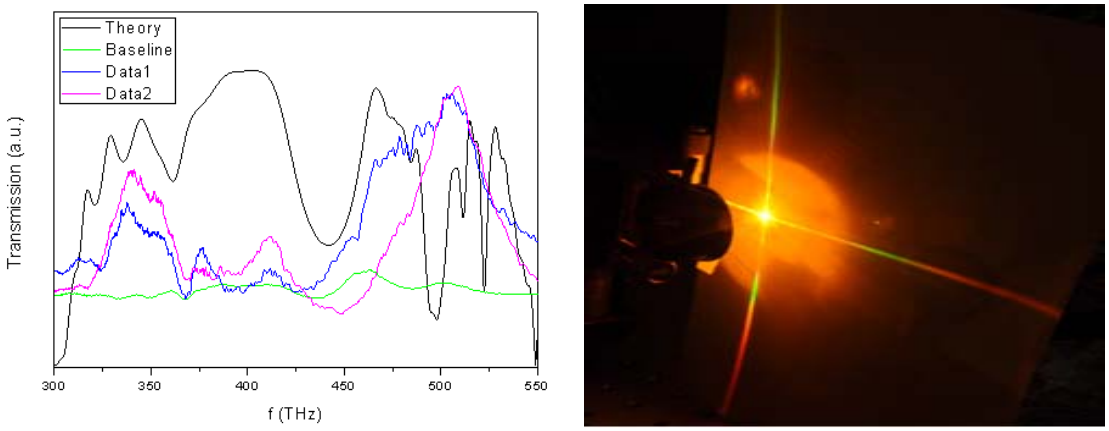

(a) (b)

Figure 21: (a) Normalized transmission diagrams for the structure of Fig. 20 (two different measurements). The image also depicts the normalized background noise (baseline) along with the theoretical simulation. (b) Characteristic diffraction pattern of the reflected wave due to the fcc geometry.

Before starting the analysis of our data we should explain how the experimental measurements were taken. Because there was lot of noise during the experiments we had to change the integration time of the spectrometer after each measurement in order to have a spectrum as smooth as possible. For that reason the transmission amplitudes of the different measurements can not be compared thus, the transmission axis is not calibrated. First we took two measurements of the intensity without placing the structure. We divided them and checked if the intensity was fluctuating a lot or if it had a constant behaviour. The resulted ratio (baseline) is shown in Fig. 21(a). Next we tried to focus the incident beam on the centre of the structure. We mentioned that the focused beam on the sample had a diameter of 24 μm while the area of the structure was 40^2 μm^2. This means that the correct alignment of the beam is not easy to be achieved since the diameter is comparable to the sample area. Thus to find the best spot, we were checking the diffraction pattern as the sample's base was moving. When the diffraction pattern colors were visible and clean (see Fig. 21(b)) the focused beam was very near to the centre of the structure. However, because we can not be sure where exactly the structure centre was, we measured the sample twice, for two different points (Data1 and Data2 in Fig. 21(a)).

Analyzing Fig. 21(a), we observe the following: Both experimental data have about the same behavior in all the frequency range we examine while the baseline follows a linear form with only small fluctuations. This means that the resulted experimental diagrams should not contain much background noise. Comparing the experimental data with the theoretical curve we can see that the agreement between them is satisfactory. From 300-450 THz the experiment follows theory with only a few deviations. However, as we move to higher frequencies (>450 THz), the experimental plots start to deviate from the theoretical curve. This phenomenon has to do with the very narrow bandgaps that are formed at higher frequencies. For example, we can observe a theoretical dip at around 500 THz. The full width at half maximum (FWHM) is about 10 THz at this dip, while the dips at 510 THz and 530 THz are even narrower. However, it is very difficult to observe so narrow peaks during an experiment, due to scattering. Thus, the spectrometer shows only a broad peak which is the superposition of all these narrow bands and gaps. In Fig. 21(b), we can see the diffraction pattern of this structure. The characteristic cross form is due to the fcc geometry of the woodpile. Additionally, we can observe that all the colors from red to green are visible. The reason for that lies to the periodicity of the structure. Only the wavelengths that are comparable with the periodicity can strongly interact with the unit cell and form a photonic gap around this frequency. For example it is clear, both theoretically and experimentally, that there is a gap around 450 THz (~665 nm). The red color has frequencies from 400-484 THz (620–750 nm). From the diffraction pattern we can see this color, which means that no transmitted wave can pass through the structure around these frequencies, explaining thus the decrease of the transmission and the formation of photonic gap.

4 Conclusion

In this work we investigated the fabrication procedure of metallic woodpile photonic crystals at the THz region. Through the sol-gel, two-photon polymerization and electroless plating metallization techniques we were able to create the appropriate polymer network, fabricate the structures in it and metallize them. We focused on the construction of woodpiles with 900 nm and 600 nm periodicity. The main achievements were the identification of threshold intensity for the discussed periodicities (2 mW and 1.85 mW respectively), the fabrication of structures with resolution below 100 nm, and the demonstration of the Ohmic behavior of metalized woodpiles through measurements of the resistance. Furthermore, we measured the transmission spectra of the structure with the smallest period and showed that the behavior was in agreement with the theoretical results at least for frequencies below 450 THz.

There are lots of experimental methods for the construction of metallic photonic crystals. The method that was followed throughout this work overpasses the others due to easy fabrication procedure and low cost materials employed.

In the last few decades there has been an increasing interest in both photonic crystals and metamaterials because of their ability to control and confine light. The greater potential applications of these structures can only be applied when they are made to function at the optical frequencies. In this work we showed that this step is feasible although more theoretical and especially experimental work is required in order to increase even more the resolution and minimize the scattering due to defects.

Bibliography

[PC1] **John D. Joannopoulos, Steven G. Johnson, Joshua N. Winn, Robert D. Meade**, *Photonic Crystals: Molding the Flow of Light*, Princeton, Princeton University Press, 1995. (2nd edition, 2008)

[PC2] **Eleftherios N. Economou**, *The Physics of Solids: Essentials and Beyond*, Heraklion, Springer Press, 2010.

[PC3] **Nader Engheta, Richard W. Ziolkowski**, *Metamaterials: Physics and Engineering Explorations*, Philadelphia, IEEE Press, 2006.

[PC4] **G. V. Eleftheriades, K. G. Balmain**, *Negative Refraction Metamaterials Fundamental Principles and Applications,* IEEE Press, 2005.

[PC5] **C. Kittel**, *Introduction to solid state physics*, California, John Willey & Sons, 1953. (8th edition, 2005)

[PC6] **J. M. Lourtioz, H. Benisty, V. Berger, J. M. Gerard, D. Maystre, A. Tchelnokov**, *Photonic Crystals: Towards Nanoscale Photonic Devices*, Orsay, Springer Press, 2003.

[PC7] **Hong-Bo Sun, Satoshi Kawata**, *Two-Photon Photopolymerization and 3D Lithographic Microfabrication*, Springer Press, 2004.

References

Chapter 1

[1] K. M. Ho, C. T. Chan, C. M. Soukoulis, Phys. Rev. Lett., **65**, 3152–3155, (1990).

[2] E. Yablonovitch, T. J. Gmitter, K. M. Leung, Phys. Rev. Lett., **67**, 2295–2298, (1991).

[3] C. T. Chan, K. M. Ho, C. M. Soukoulis, Europhys. Lett., **16** no. 6, 563–565, (1991).

[4] V. G. Veselago, Sov. Phys. Uspekhi, **10**,509, (1968).

[5] D. R. Smith, W. J. Padilla, D. C. Vier, S. C. Nemat-Nasser, S. Schultz, Phys. Rev. Lett., **84**, 4184, (2000).

[6] R. A. Shelby, D. R. Smith, S. Schultz, Science, **292**, 77, (2001).

[7] J. B. Pendry, Phys. Rev. Lett., **85**, 3966, (2000).

[8] M. Notomi, Phys. Rev. B: Condens. Matter Mater. Phys., **62**, 10696, (2000).

[9] a)C. Luo, S. G. Johnson, J. D. Joannopoulos, J. B. Pendry, Phys. Rev. B: Condens. Matter Mater. Phys., **65**, 201104, (2002). b) C. Luo, S. G. Johnson, J.D. Joannopoulos, J. B. Pendry, Phys. Rev. B: Condens. Matter Mater. Phys., **68**, 045115, (2003).

[10] S. Foteinopoulou, E. N. Economou, C. M. Soukoulis, Phys. Rev. Lett., **90**, 107402, (2003).

[11] a) S. Foteinopoulou, C. M. Soukoulis, Phys. Rev. B: Condens. Matter Mater. Phys., **67**, 235117, (2003). b) S. Foteinopoulou, C. M. Soukoulis, Phys. Rev. B: Condens. Matter Mater. Phys., **72**, 165112, (2005).

[12] E. Cubukcu, K. Aydin, E. Ozbay, S. Foteinopoulou, C. M. Soukoulis, Nature, **423**, 604, (2003).

[13] E. Cubukcu, K. Aydin, E. Ozbay, S. Foteinopoulou, C. M. Soukoulis, Phys. Rev. Lett., **91**, 207401, (2003).

[14] C. M. Soukoulis, M. Kafesaki, E. N. Economou, Adv. Mater., **18**, 1941-1952, (2006).

[15] Liang-Yu Wu, Lien-Wen Chen, J. Phys. D: Appl. Phys., **44,** 045402, (2011).

[16] Ho K. M., Chan C. T., Soukoulis C. M., Biswas R., Sigalas M., Solid State Commun., **89**, 413, (1994).

[17] Feigel A., Veinger M., Sfez B., Arsh A., Klebanov M. Lyubin V., Appl. Phys. Lett., **83**, 4480, (2003).

[18] Liu H., Yao J., Xu D., Wang P., Opt. Express, **15**, 695, (2007).

[19] Khromova I., Gonzalo R., Ederra I.,de Maagt P., J. Appl. Phys., **106**, 014901, (2009).

[20] E. Ozbay, A. Abeyta, G. Tuttle, M. C. Tringides, R. Biswas, M. Sigalas, C. M. Soukoulis, C. T. Chan, K. M. Ho, Phys. Rev. B, **50**, 1945–1948, (1994).

[21] J. Serbin, A. Ovsianikov, B. Chichkov, Opt. Express, **12,** 5221-5228, (2004).

[22] S. Y. Lin, J. G. Fleming, D.L. Hetherington, B.K. Smith, R. Biswas, K. M. Ho, M.M. Sigalas, W. Zubrzycki, S.R. Kurtz, J. Bur, Nature, **394,** 251, (1998).

[23] J.C. Knight, J. Broeng, T.A. Birks, P. St. Russel, Science, **282**, 1476, (1998).

[24] R.F. Cregan, B.J. Mangan, J.C. Knight, T.A. Birks, P. St. J. Russell, P.J. Roberts, D.C. Allan, Science, **285**, 1537, (1999).

[25] J. Broeng, S.E. Barkou, T. Sondergaard, A. Bjarklev, Opt. Lett., **25**, 96, (2000).

[26] S. Y. Lin, E. Chow, J. Bur, S.G. Johnson, J.D. Joannopulos, Opt. Lett., **40**, 1400, (2002).

[27] T.F. Krauss, Phys. Stat. Solid., A**197**, 688, (2003).

[28] E.R. Brown, C.D. Parker, E. Yablonovitch, J. Opt. Soc. Am., B**10**, 404, (1993).

[29] Sharee J. McNab, Nikolaj Moll, Yurii A. Vlasov, Opt. Express, **11**, 2927-2939 (2003).

[30] C. M. Soukoulis, ed., Photonic Crystals and Light Localization in the 21st Century (Kluwer Academic,2001).

[31] P. Lodahl, A. F. van Driel, I. S. Nikolaev, A. Irman, K. Overgaag, D. Vanmaekelbergh, W. L. Vos, Nature, **430**, 654, (2004).

[32] S. P. Ogawa, M. Imada, S. Yoshimoto, M. Okano, S. Noda, Science, **305**, 227, (2004).

[33] A. Badolato, K. Hennessy, M. Atatüre, J. Dreiser, E. Hu, P. M. Petroff, A. Imamoglu, Science, **308**, 1158, (2005).

[34] A. F. Koenderink, M. Kafesaki, C. M. Soukoulis, V. Sandoghdar, Opt. Lett., **30**, 3219-3212, (2005).

[35] W. J. Rieter, K. M. L. Taylor, H. An, W. Lin, W. J. Lin, Am. Chem.Soc., **128**, 9024-9025, (2006).

[36] H. F. Ghaemi, T. Thio, D. E. Grupp, Phys. Rev. B, **58**, 6779-6782, (1998).

[37] G. Dolling, M. Wegener, C. M. Soukoulis, S. Linden, Opt. Express, **32**, 53-55 (2007).

[38] P. R. Villeneuve, M. Piche, Progr. Quantum Electron, **18**, No.2, 153-200, (1994).

[39] J. B. Pendry, A. MacKinnon, Phys. Rev. Lett., **69**, 2772-2775, (1992).

[40] A. Lavrinenko, P. I. Borel, L. H. Frandsen, M. Thorhauge, A. Harpoth, M. Kristensen, T. Niemi, Opt. Express, **12**, 234–248, (2004).

[41] R. W. Ziolkowski, M. Tanaka, Opt. and Quantum Elect., **31**, 843–855, (1999).

[42] A. Chutinan, S. Noda, Appl. Phys. Lett, **75**, 3739–3741, (1999).

[43] A. Chutinan, S. Noda, Phys. Rev. B, **62**, 4488-4492, (2000).

[44] A. Mekis, J. C. Chen, I. Kurland, S. Fan, P. R. Villeneuve, J. D. Joannopoulos, Phys. Rev. Lett., **77**, 3787–3790, (1996).

[45] R. W. Ziolkowski, IEEE Trans. Antennas Propagat., **45**, 375–391, (1997).

[46] M. Soljacic, C. Luo, J. D. Joannopoulos, S. Fan, Opt. Lett., **28**, 637–639, (2003).

[47] E. P. Kosmidou, T. D. Tsiboukis, Opt. Quant. Electr., **35**, 931–946, (2003).

Chapter 2

[1] T. W. Ebbesen, H. J. Lezec, H. F. Ghaemi, T. Thio, P. A. Wolff, Nature, **391**, 667, (1998).

[2] W. L. Barnes, A. Dereux, T. W. Ebbesen, Nature, **424**, 824, (2003).

[3] V. G. Veselago, Sov. Phys. Solid State, **8**, 2854, (1967).

[4] J. B. Pendry, Phys. Rev. Lett., **85**, 3966, (2000).

[5] V. M. Shalaev, Nature Photon., **1**, 41–48, (2007).

[6] C. M. Soukoulis, S. Linden, M. Wegener, Science, **315**, 47–49, (2007).

[7] A. Moroz, Phys. Rev. Lett., **83**, 5274, (1999).

[8] A. L. Pokrovsky, A. L. Efros, Phys. Rev. Lett., **89**, 093901, (2002).

[9] J. Li, G. Sun, C. T. Chan, Phys. Rev. B, **73**, 075117, (2006).

[10] A. V. Akimov, A. A. Meluchev, D. A. Kurdyukov, A. V. Scherbakov, A. Holst, V. G. Golubev, Appl. Phys. Lett., **90**, 171108, (2007).

[11] Sun H-B, Kawata S., *NMR.* 3D analysis. Photopolymerization ed N Fatkullin (Berlin / Heidelberg: Springer) pp 169-273, (2004).

[12] LaFratta C. N., Fourkas J. T., Baldacchini T., Farrer R. A., Angewandte Chemie-International Edition, **46,** 6238-58, (2007).

[13] Juodkazis S., Mizeikis V., Misawa H., Journal of Appl. Phys., **106,** 051101, (2009).

[14] Maria Farsari, Boris N. Chichkov, Nat. Photonics **3**, 450 – 452, (2009).

[15] M. Farsari, M. Vamvakaki, Boris N. Chichkov, Journal of Optics, **12**, 124001, (2010).

[16] Deubel M., Wegener M., Linden S., Von Freymann G., John S., Opt. Lett., **31,** 805-7, (2006).

[17] Galajda P., Ormos P., Journal of Optics B-Quantum and Semiclassical Optics, **4,** S78-S81, (2002).

[18] Deubel M., Von Freymann G., Wegener M., Pereira S., Busch K., Soukoulis C. M., Nat. Mater., **3,** 444-7, (2004).

[19] Haske W., Chen V. W., Hales J. M., Dong W. T., Barlow S., Marder S. R., Perry J. W., Optics Express, **15,** 3426-36, (2007).

[20] Kawata, S. Sun, H.B.Tanaka, T. Takada, K. Finer, Nature**, 412**, 697–698, (2001).

[21] M. Deubel et al., Nature Mater., **3**, 444–447, (2004).

[22] F. Formanek et al, Opt. Express, **14**, 800–809, (2006).

[23] G. O. Mallory, J. B. Hajdu, "Electroless plating: Fundamentals and Applications", American Electroplaters and Surface Finishers Society, Orlando, (1990).

[24] L. J. Gerenser, Appl. Phys. Lett., **8**, 3682, (1990).

[25] Livage J., Sanchez C., J. Non-Cryst. Solids **145**, 11–19, (1992).

[26] Ro J. C., Chung I. J., J. Non-Cryst. Solids **110**, 26–32, (1989).

[27] Kline A. A., Rogers T. N., Mullins M. E., Cornilsen B. C., Sokolov L. M., J. Sol_Gel Sci. Technol. **2**, 269–272, (1994).

[28] Serbin J., Egbert, A., Ostendorf A, Chichkov B. N., Houbertz R., Domann G., Schulz J., Cronauer C., Frohlich L., Popall M., Opt. Lett., **28**, 301–303, (2003).

[29] Oubaha M., Kribich R. K., Copperwhite R., Etienne P., O'Dwyer K., MacCraith B. D., Opt.Commun, **253**, 346–351, (2005).

[30] Stevens M. P., "Polymer Chemistry: An Introduction", (New York: Oxford University Press), (1999).

[31] Allcock H. R., Lampe F. W., Mark J. E., "Contemporary Polymer Chemistry", (Upper-Saddle River, NJ: Pearson-Prentice Hall), (2003).

[32] Hiemenz P. C., Lodge T. P., "Polymer Chemistry" (New York: CRC Press), (2007).

[33] Bhuian B., Winfield R. J., O'Brien S., Crean G. M., Appl. Surf. Sci., **252**, 4845–4849, (2006).

[34] Segawa H., Yamaguchi S., Yamazaki Y., Yano T., Shibata S., Misawa H., Appl. Phys. A: Mater. Sci. Process., **83**, 447–451, (2006).

[35] Konstantina Terzaki, Nikos Vasilantonakis, Arune Gaidukeviciute, Carsten Reinhardt, Costas Fotakis, Maria Vamvakaki, Maria Farsari, Optical Materials Express, Submitted, (2011).

[36] Yun-Sheng Chen, Amir Tal, David B. Torrance, Stephen M. Kuebler, Adv. Funct. Mater., **16**, 1739–1744, (2006).

[37] A. Da Silva, C. Andraud, J. Lafait, A. Dakka, J. Phys. Condens. Matter., **12**, 4125, (2000).

[38] Z.Wang, X. Cai, Q. Chen, L. Li, Vacuum, **80**, 438, (2006).

[39] S. Link, M. A. El-Sayed, J. Phys. Chem. B, **103**, 8410, (1999).

[40] Koshiro Kaneko, Kazuo Yamamoto, Satoshi Kawata, Hong Xia, Jun-Feng Song, Hong-Bo Sun, Opt. Lett., **33**, 17, (2008).

[41] N. Takeyasu, T. Tanaka, S. Kawata, Jpn. J. Appl. Phys., Part 1 **44**, 1134, (2005).

[42] Florian Formanek, Nobuyuki Takeyasu, Takuo Tanaka, Kenta Chiyoda, Atsushi Ishikawa, Satoshi Kawata, Appl. Phys. Lett., **88**, 083110, (2006).

[43] N. Takeyasu, T. Tanaka, S. Kawata, Appl. Phys. A, **90**, 205–209, (2008).

[44] F. Formanek, N. Takeyasu, T. Tanaka, K. Chiyoda, A. Isikawa, S. Kawata, Appl. Phys. Lett., **88**, 083110-083112, (2006).

[45] Gansel J. K., Thiel M., Rill M. S., Decker M., Bade K., Saile V., von Freymann G., Linden S., Wegener M., Science, **325,** 1513-5, (2009).

[46] Varadan V. K., Jiang X., Varadan V. V., "Microstereolithography and other Fabrication Techniques for 3D MEMS", (Chichester: John Wiley & Sons), (2001).

[47] Göppert-Mayer M., Über Elementarakte mit zwei Quantensprüngen Annalen der Physik, **401,** 273-94, (1931).

[48] Kaiser W., Garrett C. G. B., Phys. Rev. Lett., **7,** 229-32, (1961).

[49] Born M., Wolf E., "Principles of Optics", (Cambridge University Press), (1999).

[50] Sauer B. B., McLean R. S., Thomas R. R., Langmuir, **14,** 3045-51, (1998).

[51] Agarwal G., Naik R. R., Stone M. O., Journal of the American Chemical Society, **125,** 7408-12, (2003).

[52] Amro N. A., Xu S., Liu G. Y., Langmuir, **16,** 3006-9, (2000).

[53] Garno J. C., Yang Y. Y., Amro N. A., Cruchon-Dupeyrat S., Chen S. W., Liu G. Y., Nano Lett., **3,** 389-95, (2003).

[54] Liang J., Scoles G., Langmuir, **23,** 6142-7, (2007).

[55] Betzig E., Trautman J. K., Science, **257,** 189-95, (1992).

[56] Heinzelmann H., Pohl D. W., Applied Physics a-Materials Science & Processing, **59,** 89-101, (1994).

[57] Samori P., Journal of Materials Chemistry, **14,** 1353-66, (2004).

Chapter 3

[1] Yu-Lin Yang, Fu-Ju Hou, Shich-Chuan Wu, Wen-Hsien Huang, Ming-Chih Lai, Yang-Tung Huang, Appl. Phys. Lett., **94**, 041122, (2009).

[2] Binping Jin, Jun Xu, Yee Kwong Pang, Wing Yim Tam, J. Opt. A: Pure Appl. Opt., **10**, 085204, (2008).

[3] Amir Tal, Yun-Sheng Chen, Henry E. Williams, Raymond C. Rumpf, Stephen M. Kuebler, Opt. Express, **15**, 18283-18293, (2007).

[4] Jiafang Li, Baohua Jia, Guangyong Zhou, Min Gu, Opt. Express, **14**, No. 22, (2006).

[5] R. Malureanu, A. Alabastri, W. Cheng, R. Kiyan, B. Chichkov, A. Andryieuski, A. Lavrinenko, Appl. Phys. A, DOI 10.1007/s00339-010-6213-z

[6] N. Tétreault, G. von Freymann, M. Deubel, M. Hermatschweiler, F. Pérez-Willard, S. John, M. Wegener, Geoffrey A. Ozin, Adv. Mater., **18**, 457, (2006).

[7] I. Staude, M. Thiel, S. Essig, C. Wolff, K. Busch, G. von Freymann, M. Wegener, Opt. Lett., **35**, No 7, (2010).

[8] A. Reiser, "Photoreactive Polymers", 1st ed. Wiley, New York, (1988).

[9] Xiaobo Yin, Nicholas Fang, Xiang Zhanga, Ignacio B. Martini, Benjamin J. Schwartz, Appl. Phys. Lett., **81**, No. 19, (2002).

[10] Quan Sun, Saulius Juodkazis, Naoki Murazawa, Vygantas Mizeikis, Hiroaki Misawa, J. Micromech. Microeng., **20,** 035004, (2010).